

Determining the impact of post-main sequence stellar evolution on the transiting giant planet population

Edward M. Bryant^{1,2*} & Vincent Van Eylen,¹

¹*Mullard Space Science Laboratory, University College London, Holmbury St Mary, Dorking, Surrey, RH5 6NT, UK*

²*Department of Physics, University of Warwick, Gibbet Hill Road, Coventry, CV4 7AL, UK*

Accepted XXX. Received YYY; in original form ZZZ

ABSTRACT

The post-main sequence evolution of stars is expected to impact the exoplanets residing on close-in orbits around them. Using photometric data from the TESS Full-Frame-Images we have performed a transit search for exoplanets with post-main sequence hosts to search for the imprints of these impacts on the giant planet population. We detect 130 short period planets and candidates, thirty-three of which are newly discovered candidates, from a sample of 456,941 post-main sequence stars spanning the evolutionary stages from the end of the main sequence to the bottom of the red giant branch. We measure an occurrence rate of $0.28 \pm 0.04\%$ for short period giant planets orbiting post-main sequence stars. We also measure occurrence rates for two stellar sub-populations, measuring values of $0.35 \pm 0.05\%$ for a sub-population representing the earliest stages of post-main sequence evolution and $0.11^{+0.06}_{-0.05}\%$ for a sub-population of more evolved stars. We show that the giant planet occurrence rate decreases with increasing stellar evolution stage, with a larger occurrence rate decrease observed for shorter period planets. Our results are clear evidence that the population of short period giant planets is being sculpted by the post-main sequence evolution of the host stars, and we conclude that this is most likely through the destruction of these giant planets through the increased strength of planet-star tidal interactions resulting in the rapid tidal decay of the planets' orbits.

Key words: planets and satellites: gaseous planets – planets and satellites: detection

1 INTRODUCTION

At the end of their main sequence life span, stars similar in mass to our Sun will undergo a period of evolution. This stellar evolution is predicted to influence the population of planets we observe around post-main sequence host stars (e.g. [Rasio et al. 1996](#); [Villaver & Livio 2009](#); [Veras 2016](#)). As the star expands during its post-main sequence evolution, we would expect a large fraction of the exoplanets discovered so far, especially those with a semi-major axis smaller than about 1 AU, to be engulfed by the expanding star ([Villaver et al. 2014](#)). However, it can be unclear what occurs during the earlier stages of the star's post-main sequence evolution, and exactly at what stage these planets begin to be destroyed by their host stars.

Close-in planets are known to interact with their host stars through tidal interactions ([Rasio et al. 1996](#)), and these interactions can result in a decay of the planet's orbit, as has been observed for the planet WASP-12 b ([Yee et al. 2020](#)). As host stars evolve off of the main sequence, one of the earliest impacts we expect is an increased rate of orbital decay due to these tidal interactions. The physics governing the dissipation of tides between the host star and an orbiting planet is complex, but the tidal dissipation is characterised as being dominated by two components: the equilibrium tide, in which the dissipation is dominated by turbulent viscosity in the outer convective envelope of the star ([Zahn 1977, 1989](#); [Esseldeurs et al. 2024](#)), and the dynamical

tide, which arises due to internal stellar oscillations which are excited by the tidal potential ([Zahn 1977, 2008](#); [Barker & Ogilvie 2010](#)).

As stars evolve off of the main sequence the stellar structure changes, primarily through the expansion of the outer layers and the deepening of the surface convection zone ([do Nascimento et al. 2012](#)). The predicted impact of post-main sequence evolution and the resulting change in stellar structure on the strength of planet-star tidal interactions has been widely studied (e.g. [Barker 2020](#); [Esseldeurs et al. 2024](#); [Weinberg et al. 2024](#)). Despite the uncertainty around the exact mechanisms which dominate the dissipation of planet-star tidal interactions, these studies all agree that the strength of these interactions is expected to increase during the post-main sequence evolution of the host star.

As such, close-in giant planets are expected to be subject to strong tidal interactions and rapid orbital decay as their host stars evolve through the sub-giant phase and up the red giant branch (e.g. [Villaver & Livio 2009](#); [Mustill & Villaver 2012](#)). We would then expect this rapid tidal decay to leave an imprint on the population of giant planets with evolved host stars. In particular, we expect a reduction in the occurrence rates of giant planets orbiting evolved stars, as compared to the main sequence giant planet population.

There have been a number of studies over recent years specifically targeting the post-main sequence stellar population. Early studies used observations from radial velocity surveys to probe this population. In these studies, the giant stars that were observed covered a wide range of super-solar masses and were used as a proxy to study how giant planet occurrence varies with stellar mass (e.g. [Johnson](#)

* E-mail: edward.bryant@ucl.ac.uk

et al. 2010; Reffert et al. 2015). Johnson et al. (2010) found the occurrence rate of giant planets to increase monotonically up to a stellar mass of $1.9 M_*$, with Reffert et al. (2015) extending the mass range and finding the giant planet occurrence rate to peak at $1.9 M_*$ and then decrease to higher stellar masses. However, the stellar masses of the stars surveyed in these studies have been called into question. Lloyd (2011, 2013) used stellar evolution models to generate a simulated galactic population, arguing that the expected mass distribution of the evolved star population should be indistinguishable from main sequence F- and G-stars. However, Johnson et al. (2013) argued that due to selection effects the evolved star sample studied in the radial velocity surveys is likely subject to a number of biases and so cannot be directly compared to the simulated population from Lloyd (2011).

Independently, Schlaufman & Winn (2013) investigated the mass distribution of the evolved star planet hosts by considering the kinematics of the host stars. Schlaufman & Winn (2013) found the Galactic UVW velocity dispersion for the planet hosting sub-giant and giant stars to be indistinguishable from a sample of F5-G5 main sequence planet hosts. They also found the velocity dispersions for the sub-giant and giant planet hosts to be larger than that for a sample of solar neighbourhood A5-F0 stars. From their results they argued that the evolved star planet hosts have a similar stellar mass distribution to the F5-G5 main sequence stars, and have on average lower stellar masses than the A5-F0 main sequence stars. From these results, Schlaufman & Winn (2013) concluded that the reduced number of short period giant planets around evolved stars (e.g. Bowler et al. 2010) is due to tidal orbital decay and not the mass of the host stars.

Planets detected around giant and sub-giant stars from the early radial velocity surveys were on long orbital periods ($P > 100$ d; e.g. Bowler et al. 2010; Reffert et al. 2015). While planets at these wide orbital distances are expected to be subject to rapid orbital evolution during the red giant phase (Villaver & Livio 2009) it is planets on much shorter orbital periods which are expected to be the most susceptible to rapid orbital decay due to tides during the early stages of post-main sequence stellar evolution (Weinberg et al. 2024).

Space based transit surveys Kepler (Borucki et al. 2010), K2 (Howell et al. 2014), and TESS (Ricker et al. 2015) have contributed to the discovery of a number of giant planets transiting post-main sequence stars with orbital periods shorter than 10 days (e.g. Lillo-Box et al. 2014; Barclay et al. 2015; Van Eylen et al. 2016; Chontos et al. 2019; Grunblatt et al. 2022). Going beyond the detection of individual planets, Grunblatt et al. (2019) used K2 photometry to study the occurrence of short period giant planets around 2476 red giant stars. Based on the detection of three planets orbiting these stars, they determined an occurrence rate of $0.49 \pm 0.28\%$ for planets larger than $1 R_J$ with orbital periods in the range $3.5 \leq P \leq 10$ days, for evolved stars with radii $R_* = 3.5 - 8.0 R_\odot$. They found this to be consistent with the occurrence of planets with similar properties orbiting main sequence stars (see e.g. Howard et al. 2012; Kunimoto & Matthews 2020; Beleznay & Kunimoto 2022). However, the limited stellar sample size available from the K2 photometry reduced the precision they could obtain for the occurrence rates. We also note that the stars targeted by Grunblatt et al. (2019) are in general more evolved than the majority of stars we study in this work and they did not probe the shortest orbital periods where we might expect to see the largest tidal impacts (Weinberg et al. 2024; Esseldeurs et al. 2024).

As a result, the question of how the early stages of post-main sequence evolution impact exoplanet systems remains largely unanswered. In particular, it remains unclear if and when planets are likely to undergo rapid orbital decay, and at what stage of their host star's evolutionary lifetime. To address these questions, we use the pho-

tometric data from the Full-Frame-Images (FFIs) delivered by the Transiting Exoplanet Survey Satellite (TESS; Ricker et al. 2015) to measure the occurrence rates of close-in planets around evolved post-main sequence host stars. The TESS FFIs provide high precision time series photometry for stars across nearly the entire sky, which have previously been used to study the occurrence of planets as a function of stellar characteristics such as stellar mass to constrain planet formation models (Beleznay & Kunimoto 2022; Bryant et al. 2023; Gan et al. 2023). Here, we study a sample of 456,941 post-main sequence stars with high-precision TESS time series photometry to constrain the occurrence of close-in giant planets, and compare this to their main sequence counterparts and to tidal theory.

We present our post-main sequence selection and sample in Section 2. The various stages of our planet search, vetting, and analysis pipeline are discussed in Section 3, before we present our planet candidate sample in Section 4. We discuss our injection-recovery tests in Section 5 and discuss how we compute the occurrence rates in Section 6. We present our occurrence rate results and discuss the implications of these results particularly in the context of the impact of post-main sequence evolution on planetary systems in Section 7, before presenting our conclusions in Section 8.

2 DEFINING THE TESS EVOLVED STAR SAMPLE

2.1 TESS Photometric Observations

The Transiting Exoplanet Survey Satellite (TESS; Ricker et al. 2015) has been monitoring the brightness of stars across the whole sky since its launch in 2018. Situated in an approximately 13 day orbit around the Earth, TESS observes a strip of the sky, with dimensions of 24 degrees \times 96 degrees, for two orbits resulting in a total of ≈ 27.4 days of observation for a given area of the sky. This 27.4 day period of observation is referred to as a sector.

During the first extended mission of TESS observations occurring between 4th July 2020 and 1st September 2022 – Sectors 27 to 55 – the TESS Full-Frame-Images were recorded at a cadence of 10 minutes. Light curves for all stars brighter than a TESS magnitude of 13.5 were produced by the Quick-look Pipeline (QLP; Kunimoto et al. 2021, 2022) and made publicly available to the community as a MAST High-Level-Science-Product¹. Full details of the QLP light curve production are provided in Huang et al. (2020), but we provide some brief details here. The QLP is a difference image photometry pipeline in which a reference image is constructed and then subtracted from each TESS image to produce a difference image. Aperture photometry is then performed on each difference image using circular apertures to compute the differential source brightness. The measured differential fluxes are converted into absolute fluxes using the TESS magnitude provided in the TIC (Stassun et al. 2019) for each source along with the TESS instrument zero-point magnitude (Vanderspek et al. 2018). This step is equivalent to deblending the flux time series and so any transit events in the QLP light curves should not be heavily impacted by dilution from nearby contaminating stars.

As light curves are made for all stars brighter than $T = 13.5$ mag, the target selection is minimal and likely to not be biased in a way that would impact an occurrence rate determination. The TESS 2 minute cadence light curve sample for example will be subject to bias due to the inclusion of Guest Observer targets, often planet or candidate host stars. Therefore due to the unbiased nature of the target selection during the production of the QLP light curves and the high quality

¹ <https://archive.stsci.edu/hlsp/qlp>

of the light curves themselves we elect to the QLP data products, for TESS sectors 27 to 55, for the systematic transit search we perform in this work. These sectors constitute the full first extended mission of the TESS satellite, during which FFIs were recorded at a cadence of 10 minutes.

2.2 Identifying Post-Main Sequence Stars

We use the TESS Input Catalogue (TIC version 8; [Stassun et al. 2019](#)) to select a sample of post-main sequence stars, using the stellar radius (R_\odot) and effective temperature (T_{eff}) values for each TIC source, which are calculated using *Gaia* DR2 photometric information ([Gaia Collaboration et al. 2018](#)). The combination of R_\odot and T_{eff} are used to identify likely evolved stars using the `EVOLSTATE` package ([Huber 2019](#)). Details of the selection are provided in ([Berger et al. 2018](#)) but in short: a PARSEC solar–metallicity stellar evolution track is used to set the terminal age main sequence boundary, and a 15 Gyr $[\text{Fe}/\text{H}] = +0.5$ dex MIST isochrone provides a lower bound to exclude main sequence binary stars. In addition to these selections, we introduce an additional MIST evolution track for a $M_* = 1.4 M_\odot$, $[\text{Fe}/\text{H}] = -0.5$ dex star to set an upper boundary for our sample. This was done to limit our sample to stars with stellar masses comparable to a main sequence sample of F and G-dwarfs. As a final cut, we impose a limit on the stellar radius of $R_* \leq 5.0 R_\odot$ and on the apparent magnitude in the TESS band of $T \leq 12$ mag. These final criteria are motivated by the need of the stars in our sample to be amenable to the detection of transiting exoplanets in the TESS data. Based on these stellar criteria we identify a full sample of 620,244 stars. Crossmatching the stellar sample obtained from this selection with the stars for which there is an available QLP 10 minute cadence light curve yields a stellar sample of 456,941 post-main sequence stars for our survey, representing 74% of the full stellar sample. We plot our post-main sequence population in Figure 1.

In this work we will consider two sub-populations for our full stellar sample. This will enable us to study how the giant planet occurrence rates change through the early stages of post-main sequence evolution. To identify these two sub-populations we use the MIST stellar evolution tracks ([Dotter 2016](#); [Choi et al. 2016](#)) to generate a boundary of equal Equivalent Evolutionary Phase (EEP, [Choi et al. 2016](#)). The MIST EEP values denote equivalent stages in the lifetime of a star across different stellar masses. For the purposes of this work, we use a EEP = 465 boundary in $[T_{\text{eff}}, R_*]$ space to split our sample into the two sub-populations (Figure 1). Using EEP as the boundary parameter provides us with two sub-populations for which the main distinguishing feature is the evolutionary stage of the stars in each sub-population. The boundary value was chosen empirically so the boundary divides the two regions of high stellar number density in $[T_{\text{eff}}, R_*]$ space (see Figure 1). The stars to the lower and left of this boundary in Figure 1 are the less evolved sub-population, which consists of 297,682 stars. We will refer to this population as the sub-giant sub-population. The stars to the upper and right of this boundary in Figure 1 are the more evolved sub-population, which consists of 159,259 stars. We will refer to this population as the early red giant sub-population.

3 PLANET SEARCH AND VETTING

3.1 Light Curve Pre-Processing

We access the QLP light curves for our sample from the MAST. For each star, we consider all sectors within the range of Sector 27 to

Sector 55 inclusive in which this star was observed together. We also exclude all time stamps with a quality flag > 0 .

The MIT Quick Look Pipeline includes a detrending step during which an iterative Kepler spline is used to flatten the light curves. We note that the node spacing for these splines is optimized for the detection of short period planets, and so short duration transits ([Huang et al. 2020](#)). Although we are searching for short period planets, due to the increased stellar radii of post-main sequence stars we expect significantly longer transit durations than would be expected for the same orbital periods around main-sequence stars. Therefore, it is likely that the transit of the planets we are searching for may be significantly distorted by the automated QLP Kepler spline. Instead, we take the undetrended QLP flux time series and employ our own light curve flattening using a biweight-estimation method ([Hippke et al. 2019](#)) using a wide window of 1.5 days. This wide-window custom flattening should enable the detection of the long (≥ 0.5 d in some cases) transits we expect for our sample.

TESS photometry contains multiple data gaps, particularly the regions between subsequent orbits and sectors. These gaps can impact window-based flattening methods such as the one we employ. Therefore, we identify any point within the light curve for a given sector where there exists a spacing of larger than 0.3 days between subsequent data points. These points are used as the boundaries to split the light curve into multiple portions with each portion being flattened independently. The TESS light curves can often display step changes in the flux across these data gaps, for example due to temperature changes when the satellite passes behind the Earth during its orbit or due to the data gaps being the result of guiding issues. These flux step changes can impact the smooth flattening method we use and so we flatten the individual portions of the light curve independently to avoid the impact of this on the final light curve. We also note that each sector is flattened independently of any other sectors.

3.2 Transit Event Detection

Following the light curve pre-processing we search for periodic transit-like signals using the Box-fitting Least Squares (BLS; [Kovács et al. 2002](#)) algorithm, as implemented in the `ASTROPY` Python library. We search initially for transiting events with periods from 0.8 – 15 days, and subsequently we then exclude any candidate with a period $P < 1$ day or $P > 12$ days. From initial analyses these extreme period ranges were found to be dominated by spurious signals. In particular the BLS detections in the longer period range were dominated by spurious detections due to the 13.7 day TESS orbit and start-/end-of-orbit systematics.

In order to consider a BLS detection as significant we require a Signal Detection Efficiency of $\text{SDE} \geq 7.3$. We also calculate a transit Signal-to-Noise ratio given by the following equation

$$S/N = \frac{\delta}{\sigma_{\text{LC}}} \sqrt{N_{\text{Tobs}}} \quad (1)$$

where δ is the transit depth, σ_{LC} is the RMS scatter of the out-of-transit region of the light curve, and N_{Tobs} is the number of in-transit flux data points. We require $S/N \geq 8.5$ for a significant detection. To determine this threshold, we consider a subset of 55,185 randomly selected stars from our input sample. For each star, we then calculate the out of transit RMS scatter in the flux. Using this RMS scatter we generate a flat light curve with flux values drawn from a Gaussian distribution with a mean of one and a standard deviation equal to the RMS scatter. We then run our BLS search algorithm on this white noise light curve. This process is repeated twenty times for each star, resulting in 1,103,700 unique simulations. Considering the

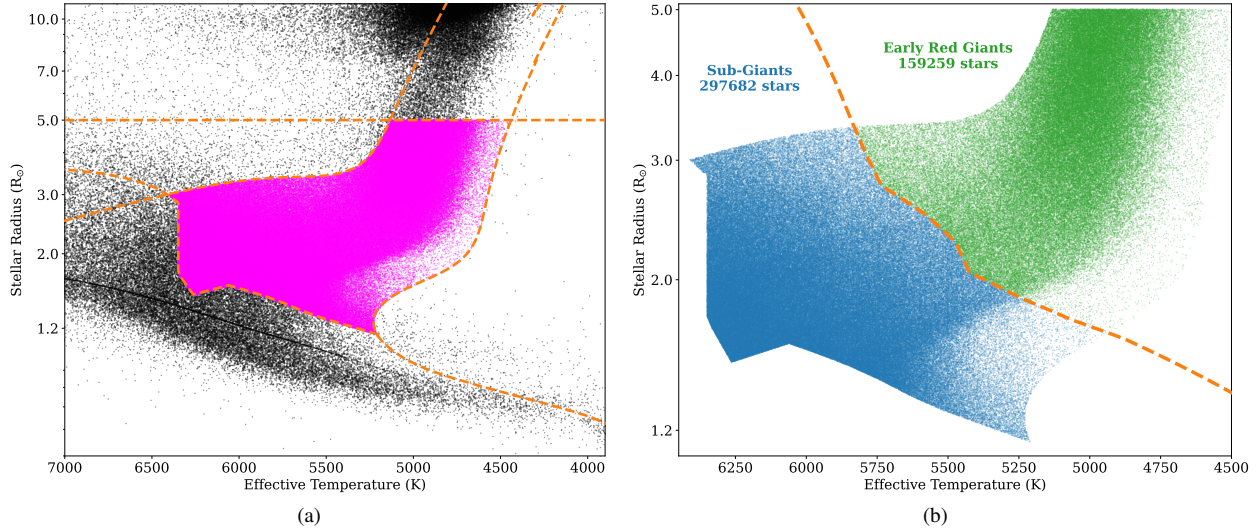


Figure 1. TESS post-main sequence stellar population used as the input sample for this study. **Left panel:** The stars included in this survey are plotted as the magenta points. The black points show a selection of stars from the TIC across all evolutionary stages as reference. The orange dashed lines show the various stellar tracks and parameter criteria used to select the sample (see Section 2.2). **Right panel:** We show the two sub-populations considered in this work. The stars in our sub-giant sample are plotted as the blue points and the stars in our early red giant sample are plotted as the green points. The orange dashed line gives the $EEP = 465$ boundary used to separate the two samples. See the text in Section 2.2 for details on this boundary. The number of stars in each sub-population are given by the annotations.

distribution of S/N values obtained for these flat light curves, the 99.99% percentile value was 8.42. From these tests, we therefore take 8.5 as the S/N threshold value to limit the false positive rate of BLS yielding detections in flat, white noise dominated light curves to less than 1 in 10,000. We also exclude any BLS detections where the measured duration of the detected event is greater than one quarter the orbital period. Our BLS search yields 17,096 significant detections of transit-like signals. We show an example of a BLS candidate detection in Figure 2.

Transit surveys often impose a requirement of a minimum of three detected transits to consider a BLS detection as a candidate planet signal. We impose a similar requirement for our search, but go one step further and require that we have three detected transits which are further than 1.5 times the transit duration reported by BLS from the start or end of a spacecraft orbit or a spacecraft momentum dump event. Both of these instances are prone to produce transit-like spurious signals due to instrumental trends in the recorded light curve. From our search, 14,860 transit candidate signals pass this subsequent criterion.

3.3 Automated False Positive Identification

Transit surveys are known to be plagued by astrophysical false positives which can produce signals that mimic the signal of a transiting planet. Primary among these false positives are eclipsing binary systems and variable stars. We therefore employ a set of quantitative vetting checks of the BLS candidates to identify any which are due to such false positive cases based purely on the TESS light curves. Here we provide details of each check performed as well as the number of candidates identified as likely false positives by each check. Note that many candidates are identified as false positives by more than one vetting check. These checks follow those presented in Bryant et al. (2023) but we have updated the algorithms used in a few cases.

In order to measure the planet occurrence rates, we employ transit injection and recovery tests in order to quantify the detection

efficiency of our transit search pipeline and vetting algorithms. During these simulations, we inject transiting planet signals into real TESS light curves, then passing those simulated transiting planet light curves through our full planet search and candidate vetting pipeline. Full details of these simulations are provided in Section 5, but here we will provide the percentage of the injected planet signals which are falsely characterised as false positives by each of our light curve vetting checks.

3.3.1 Transit Depth and Duration Measurement

The depth and duration of a transit-like event can be a clear identifier that the signal is not being produced by a transiting planet. While the BLS algorithm provides the depth and duration of the best-fitting box model, we note that these box-like models are often imperfect fits to a transit light curve. To get a more accurate assessment of the transit depth and duration we fit a trapezium-shaped model to the phase-folded transit light curve, folding the data using best orbital period and transit epoch from the BLS results. We perform the fit using a least-squares methodology, implemented using the LMFIT Python software (Newville et al. 2016). We use the transit depth, δ , reported by the LMFIT analysis to calculate the planet-to-star radius ratio using $\delta = (R_p/R_*)^2$, noting that for this initial check we do not consider the effect of limb-darkening. We then use the stellar radius of the host star, as reported in the TIC, to compute the planet radius, excluding any candidate for which we measure $R_p > 24 R_\oplus$. Using the measurement of the transit duration from the trapezium-model fit we also exclude any candidate for which the measured duration is greater than 25% the orbital period.

A total of 5,339 objects (35.93 %) are identified as likely false positives by the measurement of their transit depth. Only 0.03 % of the injected planet signals were falsely rejected by this check. A total of 2,980 objects (20.05 %) are identified as likely false positives by the measurement of their transit duration. Only 0.34 % of the injected planet signals were falsely rejected by this step.

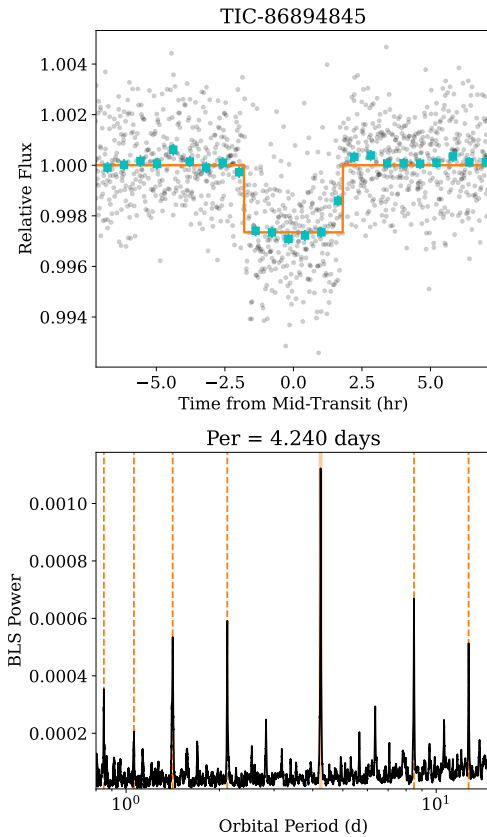


Figure 2. An example BLS candidate detection. **Top:** TESS QLP flux phase-folded at the orbital period reported by BLS, with the cyan squares showing the data binned in phase. The orange line shows the best-fit BLS box model. Note that we show a zoomed in view around phase 0 for visual clarity of the transit event. The full phase-folded flux data set extends beyond the edges of the plot. **Bottom:** The BLS periodogram for this candidate. The solid orange vertical line shows the best orbital period reported by BLS, with the dashed lines showing integer multiples and fractions of this period.

3.3.2 Stellar Density Matching

The duration of an exoplanet transit is closely related to the stellar density of the host star. Therefore, if the eclipse duration for one of our candidates is too short or long to be physically plausible for a planetary orbit around the host star, we can exclude this candidate from our sample. To do this, we use the transit parameters obtained from the BLS and vetting steps in Sections 3.2 and 3.3.1 to calculate a transit stellar density, ρ_{trans} , using Kepler's Third Law and assuming an equatorial and circular orbit. We note that for transiting planets this value will likely differ from the host star density as a result of the planet's orbit having a non-zero impact parameter or eccentricity. For the stars in our sample, many do not have reported stellar masses in the TIC and for those that do the reported stellar masses are unreliable (Stassun et al. 2019). Therefore, for each star we use the reported TIC stellar radius, R_* , to set an upper and lower boundary for the allowable range for ρ_{trans} .

Considering the lower boundary, we calculate the corresponding stellar density value for the host star radius assuming a lower stellar mass limit of $0.9 M_\odot$. An eccentric orbit can alter the transit duration and impact the stellar density measurement from the transit (Dawson & Johnson 2012; Van Eylen & Albrecht 2015). We therefore exclude any candidate for which ρ_{trans} is less than 10% of the lower boundary

stellar density value, to make sure we do not falsely exclude true planets with eccentric orbits. A total of 2493 objects (16.78 %) are excluded by this assessment. We use an upper stellar mass limit of $1.4 M_\odot$ to compute the upper boundary stellar density value. For this calculation we are assuming an equatorial orbit, and so an impact parameter $b = 0$. Orbits with $b > 0$ will result in shorter transit durations, and so this calculation is likely to yield an overestimated stellar density value. We therefore exclude any candidate for which $\rho_{\text{trans}} > 100 \times \rho_{*; \text{upper}}$, excluding 184 such candidates (1.24 %). Overall, through this stellar density analysis we exclude 2677 candidates as likely false positives (18.01 %). Only 0.13 % of the injected planet signals were falsely rejected by this step.

3.3.3 Secondary Eclipse Check

A clear signifier that the transit-like event has been produced by an eclipsing binary is the presence of a secondary eclipse – a second, shallower eclipse event seen in the light curve at the same period as the primary eclipse. To search for the presence of a secondary eclipse a series of phase values are determined which span the out-of-transit region of the light curve with a spacing of 0.005 between each phase value. We search a range of phase values in order to identify eclipsing binaries on eccentric orbits, for which the secondary eclipse will not necessarily fall at phase 0.5. At each phase value, a box-like model is fit to the phase-folded light curve, with the duration fixed to the best BLS duration. The depth of the deepest box model is recorded and used to calculate a secondary eclipse S/N using Eq. 1. Any candidate for which the secondary eclipse S/N is greater than 8 is excluded as a likely false positive. Short period giant planets may also exhibit secondary eclipses that are visible in the TESS light curves (e.g. Kabáth et al. 2022), although the secondary eclipses produced by planets will in general be shallower than those from eclipsing binaries. Giant planets on sufficiently close orbits to produce detectable secondary eclipses are also very likely to have had their orbits circularised through tidal interactions (e.g. Jackson et al. 2008) and so their secondary eclipses will be close to phase 0.5. Therefore, in order to avoid incorrectly rejecting real planets, any object with detected secondary eclipse shallower than 1 ppt and within a phase range of 0.45–0.55 is not excluded from our candidate list, as these cases may be planets.

A total of 5,835 objects (39.27 %) are identified as likely false positives by the identification of a likely secondary eclipse. Only 0.39 % of the injected planet signals were falsely rejected by this step.

3.3.4 Odd-Even Eclipse Depth Difference

If the primary and secondary eclipses of a binary system are similar in depth then the BLS algorithm can often misidentify both sets of eclipses as primary transit events, reporting half the true orbital period as the best period. In this case, the odd and even eclipses will be different depths, and we can use this depth difference to identify these eclipsing binary scenarios. For this we again fit a box-like model to the odd events and even events independently, fixing the box duration and centre time to the values reported by BLS. We then determine a depth difference S/N value using a modified version of Eq. 1 given by

$$\text{S/N} = \frac{|\delta_{\text{odd}} - \delta_{\text{even}}|}{\sigma_{\text{LC}}} \frac{1}{\sqrt{\frac{1}{N_{\text{Tobs; odd}}} + \frac{1}{N_{\text{Tobs; even}}}}} \quad (2)$$

where δ_{odd} and δ_{even} are the odd and even transit depths, $N_{\text{Tobs; odd}}$ and $N_{\text{Tobs; even}}$ are the number of in-transit data points for the odd and even transit events, and σ_{LC} is the standard deviation of the out-of-transit portion of the light curve. We identify any candidate with a S/N value greater than 8 as a likely false positive.

A total of 1,982 objects (13.34 %) are identified as likely false positives by the measurement of a likely difference in the depths of the odd and even events. Only 0.34 % of the injected planet signals were falsely rejected by this step.

3.3.5 Inter-Sector Depth Difference

Due to the large size of the TESS pixels, TESS light curves suffer from contamination from nearby stars. During the QLP light curve generation process the transit features are undiluted, assuming the transit is occurring on the target star. However, if one of the nearby stars is itself an eclipsing binary, then it will impose a transit-like signal onto the target star light curve. If the level of contamination of this nearby eclipsing binary changes between sectors then the observed transit depth will also change. This change in contamination can be due to the rotation of the TESS spacecraft meaning the stars are observed by a different camera and are located on a different part of a CCD. This can result in the PSF changing between sectors and so the contamination level also changes.

To assess the depth differences between multiple sectors, we fit the phase folded light curve for each individual sector of a given candidate using a box-like model with the timing and duration fixed to the BLS value. We then fit this box-like model to each sector to assess the transit depth. To assess whether there is a significant inter-sector depth difference we calculate a signal-to-noise value for the depth difference between the deepest and shallowest sector depths given by

$$S/N = \frac{\delta_{\text{max}} - \delta_{\text{min}}}{\sigma_{\text{LC}}} \frac{1}{\sqrt{\frac{1}{N_{\text{Tobs; max}}} + \frac{1}{N_{\text{Tobs; min}}}}} \quad (3)$$

where δ_{max} and δ_{min} are the maximum and minimum individual sector transit depths, $N_{\text{Tobs; max}}$ and $N_{\text{Tobs; min}}$ are the number of in-transit data points for these two transit events. We identify any object with a S/N value greater than 8 as a likely false positive.

A total of 2,913 objects (13.96%) are identified as likely false positives by the measurement of a significant difference between the eclipse depths measured in different sectors. Only 1.25% of the injected planet signals were falsely rejected by this step.

3.3.6 Eclipse Phased Variability

This check searches for variability in the light curve in phase with the orbit of the companion. Such phased variability is a signifier the transit-like event is caused by a stellar companion. We determine the R^2_{Harmonic} value, following [Montalto et al. \(2020\)](#), but see also Eqs. 1 and 2 of [Bryant et al. \(2023\)](#) for details. We exclude any object with $R^2_{\text{Harmonic}} > 0.6$ as a false positive. A total of 1,036 objects (6.97 %) are identified as likely false positives by the identification of variability phased with the eclipse events. Only 0.02 % of the injected planet signals were falsely rejected by this step.

3.3.7 Lomb-Scargle Analysis

Continuously varying stars can often be erroneously identified by the BLS algorithm as periodic transit-like signals. We employ a number of techniques to identify these objects. These algorithms are the same

as those employed in [Bryant et al. \(2023\)](#), and so we refer the reader there for details on the implementation. Here we simply report on the thresholds used in this instance and the numbers of objects identified by each check.

As a first check to identify variable stars we compute a Generalised Lomb-Scargle (GLS; [Lomb 1976](#); [Scargle 1982](#)) periodogram of the out-of-transit portion of the light curve, excluding any object which yields a GLS power greater than 0.3 as a false positive. A total of 3,175 objects (21.37 %) are identified as likely false positives by the presence of a significant peak in the Lomb-Scargle periodogram of the out-of-transit portion of the light curve. Only 0.15 % of the injected planet signals were falsely rejected by this step.

3.3.8 Excess Scatter Analysis

For the out-of-transit portion of the phase folded light curve we compare the RMS flux scatter to the RMS of the point-to-point flux scatter to determine the σ_{excess} value as defined in Eq.3 of [Bryant et al. \(2023\)](#). A value of σ_{excess} different to unity signifies the presence of continuous variability in the light curve. We exclude any object with $\sigma_{\text{excess}} < 0.4$ or $\sigma_{\text{excess}} > 1.3$ as a false positive. A total of 2,816 objects (18.95 %) are identified as likely false positives by the measurement of an increased root mean square scatter of their light curves in comparison to the point-to-point light curve scatter. Only 0.06 % of the injected planet signals were falsely rejected by this step.

3.3.9 Light Curve Asymmetry Test

We determine the asymmetry of the phase folded light curve following the prescription of [Bryant et al. \(2023\)](#). For this we compare the RMS point-to-point scatter of the phase-folded light curve running from phase -0.5 to 0.5, with the light curve folded using the absolute values of the phase, to run from 0.0 to 0.5. We calculate the ratio of scatters of the absolute phase folded light curve to the standard folded light curve, excluding any object for which this ratio is less than 0.8 or greater than 1.3 as a false positive. A total of 812 objects (5.46 %) are identified as likely false positives by the measurement of a significant asymmetry in their out-of-transit light curves. Only 0.01 % of the injected planet signals were falsely rejected by this step.

3.3.10 Increased Scatter During Transit

In addition to astrophysical false positive scenarios, the BLS algorithm can also detect spurious signals from non-astrophysical sources as periodic signals. Occasionally the BLS algorithm can incorrectly identify regions of high scatter, in particular systematic decreases in flux, as transit events. To identify these cases, first we compute the flux residuals to the best fit trapezium model. We calculate the RMS point-to-point scatter of the flux residuals for the in-transit, pre-transit, and post-transit portions of the light curve. We then calculate the ratios of the in-transit scatter value to pre-transit value and post-transit values. We exclude any object for which either of these two ratios is greater than 5.

A total of 513 objects (3.45 %) are identified as likely false positives by the measurement of an increased scatter during the in-transit portion of the light curve. Only 0.003 % of the injected planet signals were falsely rejected by this step.

Table 1. Parameter Priors for Transit Fitting

Symbol	Prior
T_C	$\mathcal{U}(T_C; \text{BLS} - 0.05 \times P_{\text{BLS}}, T_C; \text{BLS} + 0.05 \times P_{\text{BLS}})$
P	$\mathcal{U}(0.95 \times P_{\text{BLS}}, 1.05 \times P_{\text{BLS}})$
R_P/R_*	$\mathcal{U}(0, 1)$
a/R_*	$\mathcal{U}(1.1, \infty)$
i	$\mathcal{U}(0, 90)$
q_1, q_2	$\mathcal{U}(0, 1)$

3.3.11 Near data gap event check

Transit searches in TESS observations in particular are impacted by systematics which arise at the start and end of data gaps due to the spacecraft orbit. These systematics often arise from increased scattered light on the detector, imperfect flux detrending at these points, or a combination of both these effects. We therefore determine whether the BLS phase-fold signal is dominated by events near these data gaps, and so are likely dominated by spurious signals. To do this we extract the log-likelihood values for each transit event as computed by the BLS algorithm. We then calculate the total log-likelihood contributions from the events near the data gaps, $\ln L_{\text{edge}}$, and those which are firmly within the TESS data chunks, $\ln L_{\text{body}}$. If $\ln L_{\text{body}} \leq 0$ we automatically exclude the object, and if $\ln L_{\text{edge}} \leq 0$ the object automatically passes this check. If both values are positive and non-zero we then calculate the ratio $\ln L_{\text{edge}} / \ln L_{\text{body}}$ excluding any object for which this ratio is greater than 3.

A total of 488 objects (3.28 %) are identified as likely false positives due to the fact that their BLS detections are dominated by events which occur close to a data gap or momentum dump event. Only 0.01 % of the injected planet signals were falsely rejected by this step.

3.3.12 Overall Light Curve Vetting Results

Overall, out of the 14,860 objects containing periodic signals identified as transit-like candidates using BLS, our light curve vetting algorithms identify 11,310 (76.11 %) of them as likely false positive scenarios. This leaves 3,550 objects which remain as possible transiting planet candidates. For the transiting planet signals we simulate for the injection and recovery tests (see Section 5 for details) just 2.38 % of them are rejected in total by our light curve vetting algorithms. Therefore, while there will be a small number of genuine planets misclassified as false positives by these checks, the majority of the 11,310 objects rejected will be true false positives.

3.4 Transit Fitting Analysis

3.4.1 Transit Model

The next stage of the candidate selection pipeline is to perform a transit fitting analysis for the candidates which pass the light curve vetting stage. We perform this analysis to obtain a more accurate estimate of the radius and impact parameter of the companion. For this we use the emcee package (Foreman-Mackey et al. 2013) to perform a Markov Chain Monte Carlo (MCMC) analysis.

We use the BATMAN package (Kreidberg 2015) to generate the transit models at each step of the MCMC sampling using the following as free parameters: the reference mid-transit time, T_C , the orbital period, P , the planet-to-star radius ratio, R_P/R_* , the semi-major axis of the orbit scaled to the stellar radius, a/R_* , and the orbital inclination, i . For the stellar limb darkening we use the quadratic law fitting for the

q_1 and q_2 parameters following the Kipping (2013) parameterisation for the limb-darkening coefficients. We also fit for an out-of-transit flux offset, f_0 , such that the out-of-transit flux baseline is equal to $1 + f_0$. We have a total of eight free parameters for this analysis. For all parameters we use uniform priors such that we ensure physically realistic transit models but do not bias the results of the analysis in any way. We provide the exact prior ranges used in Table 1. We run 20 independent chains for a burn-in phase of 5,000 steps per chain followed by a sampling phase of 50,000 steps per chain, resulting in a total of 1 million posterior samples for each candidate.

From this transit analysis we apply a further set of candidate selection criteria, using the posterior distributions. First, we identify the radius ratio which gives the highest log likelihood value, and use this along with the TIC stellar radius to calculate the best-fit planet radius $R_{P; \text{Best}}$. We then exclude any candidate with $R_{P; \text{Best}} > 22 R_{\oplus}$ as a likely eclipsing binaries. We also include a check to exclude any candidate with $R_{P; \text{Best}} = 0$, although we note that the lowest $R_{P; \text{Best}}$ value for any candidate is $1.36 R_{\oplus}$, and so no candidates are excluded by this lower limit. We also compute the duration of best-fitting transit model, and exclude any candidate for which this transit duration is greater than 25% of the best-fit orbital period. Next, we use the posterior distributions of a/R_* and i to compute a posterior distribution for the impact parameter b . We then exclude any candidate for which either the median or best-fit b values are greater than 0.9. Finally, we use our parameter posterior distributions to compute a posterior distribution for the transit stellar density, ρ_{trans} . For each object we also compute a lower and upper stellar density value for each object using the same method as in Section 3.3.2. If the 95th percentile value of the ρ_{trans} posterior is less than $0.1 \times \rho_{*, \text{lower}}$ or if the 5th percentile value is greater than $10 \times \rho_{*, \text{upper}}$ we exclude the candidate. Note the tighter upper boundary as compared to when considering ρ_{trans} in the light curve vetting stage. This is because while we are still assuming a circular orbit we are no longer assuming an equatorial orbit (i.e. $b = 0$) in the calculation of ρ_{trans} . From this transit fitting analysis we identify 2,186 of our candidates as likely false positives, leaving a sample of 1,364 planet candidates. For the 10,000 injected transiting planets we apply our transit fitting analysis to 6.4 % of them were falsely labelled as false positives.

3.4.2 Flat Line, Sinusoidal, and Odd-Even Eclipse Models

We perform additional modelling analyses to assess whether a planet transit model best describes the light curves of each object. To assess this we fit each light curve with additional models. The first of these is a flat line model, governed by a single parameter, C_{flat} , to assess whether the data warrants the inclusion of a transit model. We fit for just a single free parameter: the constant flux level, C_{flat} . The second is a sinusoidal model, to further assess whether the light curve is better explained by a transit model or a continuous variability like model. For the sinusoid model, the phase of the sinusoid is fixed such that a minimum of the sinusoid occurs at phase 0. We consider five possible sinusoid periods for each object: the detected BLS period for the candidate, along with the second, third, fourth, and fifth harmonics of this period. For each sinusoid period, we fit for the semi-amplitude of the sinusoid, A , as well as the flux baseline level, C , as free parameters, selecting the period which yields the highest log likelihood value as the best sinusoidal model.

For all analyses performed here we sample the parameters using an MCMC process using the emcee package, running eight independent walkers for 3,000 burn-in steps, followed by 15,000 samples per walker. We then use the Bayesian Information Criterion (BIC) to assess whether a transit-like model is warranted by the light curve

over either the flat line or sinusoidal models. The BIC for a given model is calculated using the equation

$$\text{BIC} = k \ln n - 2 \ln \mathcal{L}, \quad (4)$$

where k is the number of parameters, n is the number of data points, and \mathcal{L} is the maximum log likelihood value obtained for a given model. For the transit model we use $k_{\text{trans}} = 8$, for the sinusoidal model we use $k_{\text{sinusoid}} = 4$, and for the flat line model we use $k_{\text{flat}} = 1$. We note that the model which is preferred yields the lowest BIC value, with a BIC difference of greater than 10 denoting strong evidence in favour of a particular model (Neath & Cavanaugh 2012). As such, for an object to remain in our candidate sample it must satisfy these two criteria

$$\text{BIC}_{\text{FlatLine}} - \text{BIC}_{\text{Transit}} \geq 10, \quad (5)$$

$$\text{BIC}_{\text{Sinusoid}} - \text{BIC}_{\text{Transit}} \geq 10. \quad (6)$$

We also consider the scenario in which the light curve is better explained by an eclipsing binary scenario in which the odd and even eclipses are different depths. To assess this we perform a further round of transit fitting analysis using the same models and modeling prescription as in Section 3.4.1. The one difference is an alteration to the prior used for T_C , where for this analysis we use a uniform prior between $T_{C\text{Best}} \pm 0.5 \times \text{Dur}_{\text{Best}}$, where $T_{C\text{Best}}$ and Dur_{Best} are the best fit mid-transit time and transit duration from the analysis performed in Section 3.4.1.

During this analysis we perform two MCMC sampling processes, one for the odd eclipse events and one for the even eclipse events. We then take the sum of the maximum log likelihood values from these two sampling processes along with a number of parameters $k_{\text{odd-even}} = 16$ to compute the BIC for the Odd-Even eclipse model. In this instance, we consider $\Delta\text{BIC} = \text{BIC}_{\text{Transit}} - \text{BIC}_{\text{OddEven}}$ and exclude any object with $\Delta\text{BIC} > 10$ as a likely false positive. We also extract the best fit radius ratio values for each eclipse, $R_P/R_{*{\text{Odd}}}$ and $R_P/R_{*{\text{Even}}}$, and compute the ratio of these two values. We then further exclude any object for which this ratio is less than 0.5 or greater than 2.

From these further modelling analyses we identify a further 657 candidates as likely false positives, leaving a planet candidate sample of 707 candidates. Of the 9,360 injected planets labelled as planet candidates by the transit fitting analysis 4.84 % are incorrectly labelled as false positives by the additional modelling analyses.

3.4.3 Individual Sector Transit Fitting

In order for any of the 707 planet candidates to remain as high quality transiting planet candidates, the transit signal must persist across all TESS sectors. To assess this for our candidates we fit all available QLP light curves for each candidate, fitting each sector individually. We downloaded the QLP light curves for each star using the LIGHTKURVE software (Lightkurve Collaboration et al. 2018). The fitting process used is the same as in Sector 3.4.1, except we now use a burn-in phase of 3,000 steps per chain and a sampling phase of 20,000 steps per chain.

From this analysis, we employ two checks to identify likely false positives. First, at each step in the sampling process we calculate the transit depth, δ , of the model. Any objects for which more than 20% of the MCMC samples from any individual sector yield $\delta = 0$ are rejected as false positives. These scenarios are most likely cases where systematic events during one or a small number of sectors,

such as a high amount of scattered light, produces a spurious signal which in the phase fold can be mistaken for a transit signal. However, such a signal would not be seen in all sectors.

For the second check, we identify objects for which the measured transit depth from the MCMC varies significantly between sectors. To do this we calculate the following quantity

$$\text{Median} \left(\frac{|\delta_i - \text{Median}(\delta_i)|}{\sigma_{\delta_i}} \right), \quad (7)$$

where δ_i is the transit depth measured for an individual sector and σ_{δ_i} is the transit depth uncertainty. In words, we calculate the absolute difference of each individual sector transit depth from the median of all the individual sector transit depth values. This difference is then weighted by the uncertainty in the individual transit depth. We then take the median of these values as our metric. Any candidate for which this metric is greater than three we take as showing a high level of transit variability characteristic of a false positive scenarios. This second check can identify nearby blended eclipsing binary scenarios (see Section 3.3.5), spurious signals such as those caused by high scattered light events, or signals produced by stellar variability, for which the variability signal and amplitude can vary on a timescale of months to years.

Using this analysis we identify a further 260 false positives from our candidate list, leaving a sample of 447 planet candidates. Considering the injection and recovery simulations, 3.2% of the injected planets for which the individual sector fitting analysis was performed were falsely labelled as false positives.

3.5 Final Candidate Checks

3.5.1 Blend Scenario Final Analysis

The TESS pixels are 21 " on each edge. Therefore, light curves generated from the TESS full frame images can suffer from contamination from nearby stars. If these nearby stars are themselves eclipsing binaries, this can result in apparent transit events being observed for the target. A crucial step in TESS planet searches is to identify and remove these nearby blend cases.

To do this, we use the TRANSIT-DIFFIMAGE tool² to produce difference images for the transit events observed for our candidates. We use TRANSIT-DIFFIMAGE to determine the centroid location of the difference image for each sector using a Pixel Response Function (PRF) modeling approach. We then compare the PRF centroid position of the difference image to the catalog pixel position of the target at the time of the TESS observations. Any object for which the PRF centroid position is offset from the target position by greater than 1 pixel is excluded as a likely nearby blend. Out of the 447 planet candidates which pass the transit fitting analysis, 236 are identified and excluded as likely nearby blends based on the PRF centroid analysis, leaving a sample of 211 planet candidates.

Nearby blended scenarios can also be identified using the TESS-POSITIONALPROBABILITY code (Hadjigeorgiou & Armstrong 2024), which quantifies the probability that each star in the TESS image surrounding the target could be the real source of the observed signal. However, currently TESSPOSITIONALPROBABILITY only works using light curves from the SPOC pipeline. For this study, 171 of the remaining 211 candidates do have a TESS-SPOC FFI light curve available (Caldwell et al. 2020) and so we run TESSPOSITIONALPROBABILITY for this subset of our candidates. We reject any object

² <https://github.com/stevepur/transit-diffImage>

for which the target star does not have the highest probability as a likely false positive, thereby identifying and excluding a further 34 candidates as likely nearby blends.

Combined, these nearby blend checks identify a total of 270 likely blended false positive scenarios, leaving us with 177 high quality, likely on target, transit planet candidates.

3.5.2 Gaia Non-Single Stars

The *Gaia* mission (Gaia Collaboration et al. 2018, 2023) released a catalogue of non-single stars (NSS) as a part of its third data release³. We cross-matched our target list with this catalogue to identify whether any of our candidates have been found to be stellar multiple systems. We find thirteen objects identified as NSS, although two of these (TIC-29119552 and TIC-148340346) are identified with periods longer than 100 days and a further three (TIC-155858369, TIC-386699314, and TIC-397510904) simply show long term astrometric or spectroscopic trends indicative of a wide stellar companion. Such stellar multiples will not mimic the observed transit signals and will not preclude these target stars from also hosting short period planets, and so we do not remove these from our candidate list. However, seven of our candidates (TIC-46627823, TIC-72556406, TIC-165493409, TIC-231279168, TIC-231630147, TIC-289539327, and TIC-449050248) are listed as NSS with the *Gaia* NSS period matching the period of our planet candidate. We therefore identify these systems as eclipsing binaries and remove them from our candidate list. One further candidate (TIC-231630147) is listed as an NSS with a period of 44.85 days. While this does not match the period of the planet candidate, a stellar companion at such a period would very likely prohibit the formation and stable orbit of any planet at a close orbital distance, and so we also remove this candidate from our sample. Overall, we exclude eight candidates from our sample based on the *Gaia* NSS information, leaving 169 planet candidates.

Further to this, thirteen of our candidates are reported as eclipsing binary or stellar multiple false positives by the TESS Follow-Up Team via ExoFoP⁴. We remove these thirteen from our candidate list, leaving 156 planet candidates.

3.5.3 Visual Light Curve Inspection

As a last check, we now manually inspect the light curves of the remaining objects, to determine if any are clear false positives which evaded the automatic checks deployed in this work. We first visually inspect the 10 min cadence QLP light curves for our candidates. We find ten of our candidates to be likely false positives, and so exclude them from our sample. The light curves of these ten candidates display either continuous variability, odd-even depth differences, or secondary eclipses which show the objects to be variable stars or eclipsing binaries. While these signals are visible to the eye they do not meet the signal-to-noise thresholds to be identified by our automated light curve vetting. For one further candidate - TIC-45047401 - our visual inspection reveals the presence of just a single clear transit event. While this may still be a true planet, the true orbital period will be significantly longer than our 12 day upper limit. Therefore we also excluded TIC-45047401 from our candidate sample.

After this we now visually inspect all the QLP, TESS-SPOC FFI,

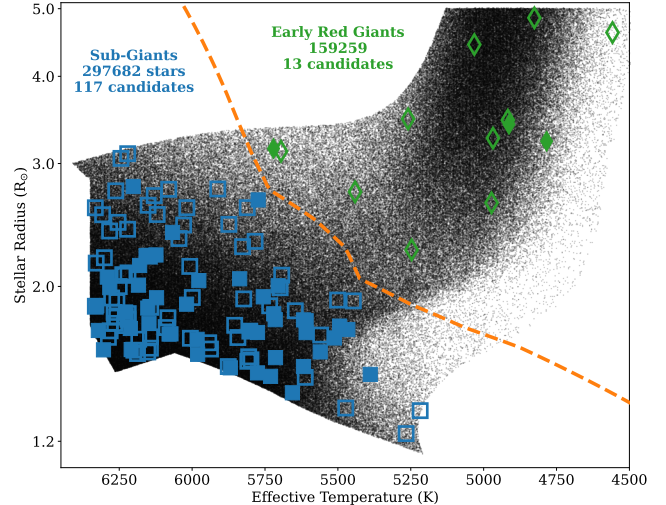


Figure 3. Host stars of the 130 planet candidates detected using our planet search and vetting pipeline. The 117 host stars within our sub-giant sub-population are plotted as the blue squares, and the 13 host stars within our early red giant sub-population are plotted as the green diamonds. Filled in symbols highlight host stars of confirmed planets (according to the NASA exoplanet archive), and open symbols highlight those stars which host planet candidates which are yet to be confirmed. Our full stellar sample is plotted as the black points and the orange line shows the $EEP = 465$ boundary we use to separate the two sub-populations (see Section 2.2).

and SPOC 2 minute cadence light curves which exist for our remaining 145 candidates. Similar to the analysis performed in Section 3.4.3 we are primarily checking to ensure a consistent transit signal is observed across all sectors and light curve extraction pipelines. Through this inspection, we identify fifteen of our candidates as likely false positives, and remove them from our candidate sample. This leaves us with a final sample of 130 planet candidates. We plot the host stars of our candidates in relation to our overall input stellar sample in Figure 3.

4 PLANET CANDIDATE SAMPLE

Out of our 130 planet candidates, a selection of 48 of our candidates are already known planets present in the NASA exoplanet archive⁵. A further 49 are reported as candidates in the TESS Objects of Interest (TOI) catalogue (Guerrero et al. 2021). This leaves 33 new candidates not yet reported to the community. We plot the phase-folded QLP light curve for each of the 33 new planet candidates we detect in Figure B1. We plot the orbital periods and radii of all 130 of our planet candidates in Figure 4 and provide details on them and their host stars in Tables A1, A2, A3, and A4. From Figure 4 we can see that the bulk of our detected planets and candidates sit at orbital periods longer than approximately 3 days, with only a few planet candidates seen at short orbital periods $P \leq 2$ days. This is in contrast to the current known population of primarily main sequence stars for which there is a decent sized population of giant planets at these short periods. This already is suggesting that strong tidal interactions may be at play for our post-main sequence population (e.g. Barker 2020; Esseldeurs et al. 2024; Weinberg et al. 2024), although we will need

³ https://gea.esac.esa.int/archive/documentation/GDR3/Gaia_archive/chap_datamodel/sec_dm_non-single_stars_tables/

⁴ <https://exofop.ipac.caltech.edu/tess/>

⁵ <https://exoplanetarchive.ipac.caltech.edu/index.html>; accessed on 4th March 2025

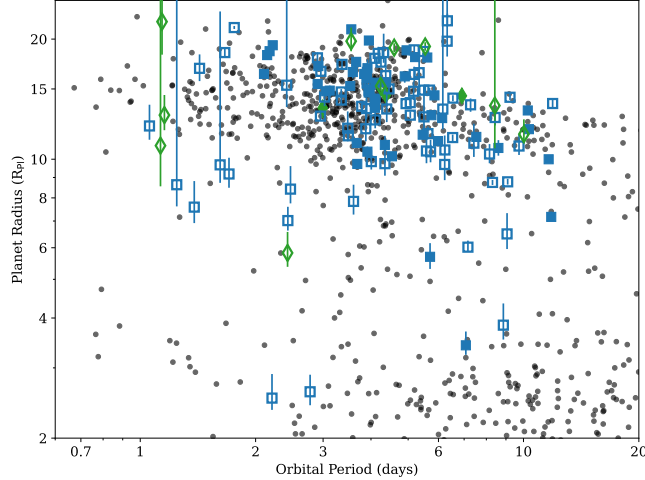


Figure 4. Our post-main sequence sample of planets and planet candidates. As with Figure 3, planets and candidates around stars in our sub-giant sub-population are plotted as the blue squares and those around stars in our early red giant sub-population are plotted as the green triangles. Confirmed planets (according to the NASA exoplanet archive) are plotted as the filled symbols and open symbols show as yet unconfirmed planet candidates. The black points show the population of known planets from the NASA exoplanet archive with a planet mass and radius measured to better than 40 % precision.

to compute the occurrence rates before drawing strong conclusions about the population demographics.

4.1 False Positive Probabilities

Despite our extensive vetting of our planet candidates, there will remain some false positives within our planet candidate sample. For the calculation of the planetary occurrence rates, we therefore now estimate a False Positive Probability (FPP) for each of our candidates. For the candidates in our sample which have been independently published as confirmed objects, we assign $FPP = 0$. For the remaining candidates, we estimate the FPP values using the TRICERATOPS software (Giacalone & Dressing 2020; Giacalone et al. 2021). TRICERATOPS is a Python code which simulates a range of possible transiting planet or eclipsing binary scenarios which could produce the observed transit signal, and then calculates the relative probabilities of each scenario for a given target star. Using these scenarios and probabilities, each candidate is then assigned a FPP value. For the 82 candidates for which we calculate a TRICERATOPS FPP value we obtain a mean FPP value of 0.41. Of these 82 candidates, 30 have a value of $FPP > 0.5$.

5 INJECTION-RECOVERY SIMULATIONS

We utilise planet injection-recovery simulations to quantify the detection efficiency of our pipeline. This is a vital step in converting our population of planet candidates into an overall occurrence rate estimation. As has been performed during previous planet population studies (e.g. van Sluijs & Van Eylen 2018; Bryant et al. 2023) we simulate and inject planet transits into real TESS light curves. We use as our base light curves the 408,758 stars from our initial input sample which did not yield a significant BLS detection. For each of these stars we simulated four transiting planet signals, giving us a total of 1,635,032 injected planet light curves.

We applied our full transit search and light curve vetting algorithms (Sections 3.2 and 3.3) to all simulated light curves. Due to computational constraints we are unable to perform a full transit fitting analysis on all 626,330 simulated objects which pass the BLS and light curve vetting stages. However, to assess the performance of our light curve fitting stages we instead randomly select a set of 10,000 simulated light curves, performing our full transit fitting analysis (Section 3.4) on this subset.

We provide the results of these tests for our full stellar sample in Figure 5 and for our two sub-populations independently in Figure 6, plotting our pipeline detection efficiency as a function of planet period and radius. From these results we can see that the pipeline detection sensitivity decreases to lower radii, and is significantly reduced for small radii, $R_P \leq 8R_\oplus$, especially for the early red giant sub-population. Therefore, while before now we have not introduced a lower limit on the planet radius in our planet search, when determining the occurrence rates we focus on the giant planet population, considering only planets with $R_P \geq 8R_\oplus$.

Of our 130 planets and planet candidates, for twelve we measure $R_P \leq 8R_\oplus$, including three previously known planets: HD 89345 b (TIC-350020859; Van Eylen et al. 2018), TOI-329 b (TIC-169765334; Polanski et al. 2024), and TOI-1736 b (TIC-408618999; Akana Murphy et al. 2023), and four TOI candidates: TOI-1291.01 (TIC-198186769), TOI-5069.01 (TIC-381360757), TOI-5177.01 (TIC-350033870), and TOI-5645.01 (TIC-366804698). While we do not include these twelve planets and candidates in our occurrence rate analysis we do include details on them and their host stars in Table A4.

6 OCCURRENCE RATE DETERMINATION

We now determine the planet occurrence rates for our post-main sequence stellar population using our sample of detected planet candidates and the detection efficiencies we determine using our injection-recovery tests. We calculate the occurrence rate, $f_{\text{occ}} = n_{\text{pl}}/N'$, where n_{pl} is the number of detected planets and N' is the number of stars amenable to the detection of an exoplanet (see Bayliss & Sackett 2011; Gan et al. 2023; Bryant et al. 2023). We use our estimated false positive probability (FPP) for each candidate (see Section 4.1) to compute n_{pl} as

$$n_{\text{pl}} = \sum_i (1 - FPP_i). \quad (8)$$

N' is calculated using the results of our injection-recovery simulations as

$$N' = N_* \frac{\sum_{i=1}^{N_*; \text{ sim}} \delta_{\text{det},i} \mathcal{P}_{\text{tr},i}}{\sum_{j=1}^{N_*; \text{ fit}} \delta_{\text{fit},j}}, \quad (9)$$

where N_* is the number of stars in the input sample, $N_*; \text{ sim}$ is the total number of simulated planet light curves, $N_*; \text{ fit}$ is the number of simulated light curves included in the transit fitting analysis, $\delta_{\text{det},i}$ is a detection delta function equal to one if a given simulated planet was detected as a candidate by the BLS (Section 3.2) and labelled as a planet candidate by the light curve vetting (Section 3.3) or zero otherwise, $\delta_{\text{fit},i}$ is a similar detection delta function but for the transit fitting analysis (Section 3.4), and $\mathcal{P}_{\text{tr},i}$ is the geometric probability that a given injected planet would transit. This transit probability is given as

$$\mathcal{P}_{\text{tr},i} = 0.9 \times \frac{R_*}{a}, \quad (10)$$

where R_P is the radius of the injected planet, R_* is the stellar radius

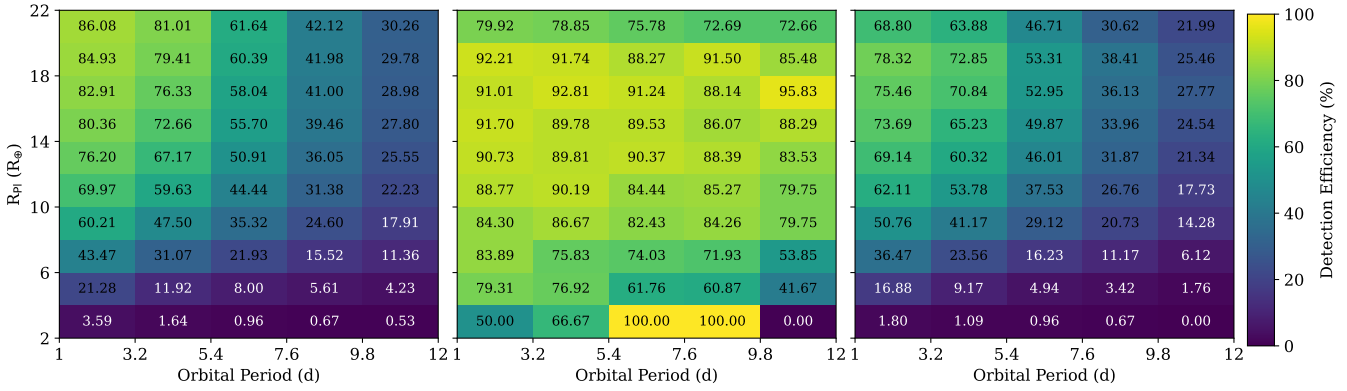


Figure 5. Detection efficiency of stages of our planet search and vetting pipeline. The three panels show the detection efficiencies for: **left:** our full planet search and automated light curve vetting (see Sections 3.2 and 3.3); **middle:** our complete transit fitting analysis (see Section 3.4); **right:** the combined performance of the complete planet search, vetting, and fitting analysis pipeline. The colour of the grid cells gives the detection efficiency (%) for planets within the cell. The numbers in each box also give the percentage detection efficiency within each grid cell.

of the host, and a is the semi-major axis of the orbit. The factor of 0.9 is applied as in our search we only consider as a planet any candidate for which our transit fitting analysis yields an impact parameter of $b \leq 0.9$.

We know that giant planet occurrence rates are dependent on the orbital period, P , and radius of the candidate, R_p , (e.g., [Kunimoto & Matthews 2020](#)) and from Figure 5 we see that our detection efficiency also depends on P and R_p . Therefore, when computing the occurrence rates we split up the planet candidate and injected planet samples into a grid in orbital period and planet radius. For each $[P, R_p]$ grid cell we then compute number of detected planets, their false positive probabilities, and the N' value.

To assess the uncertainty in our occurrence rate calculations, we perform a bootstrapping analysis. For this, we randomly draw 1000 sets of stars from our input sample. These randomly drawn stellar samples consist of 456,941 stars, the same size as the initial stellar sample, and are drawn with replacement. We then compute the occurrence rates using our approach above for each random sample. From the set of occurrence rate samples we then compute the 16th and 84th percentile values, taking the difference between these values and our measured occurrence rate value as the 1σ uncertainty value on the occurrence rate.

We note that these calculations are performed independently for each $[P, R_p]$ grid cell. For any grid cell in which we have no detected planet candidates, or only planet candidates with $1 - \text{FPP} < 10^{-4}$, we instead take the occurrence rate value to be equal to zero with an upper uncertainty obtained by calculating the 68th percentile upper limit. We calculate these upper limits following [van Sluijs & Van Eylen \(2018\)](#) who note that the occurrence rate upper limit can be calculated using

$$f_{\max}(P, R_p) = 1 - (1 - C)^{\frac{1}{N'(P, R_p) + 1}}, \quad (11)$$

where C is the confidence level for the upper limit.

7 RESULTS AND DISCUSSION

7.1 Post-Main Sequence Occurrence Rates

Using the results from our planet search and vetting we measure a short period, giant planet ($1 \leq P \leq 12$ d and $8 \leq R_p \leq 22 R_\oplus$) occurrence rate value of $0.28 \pm 0.04\%$ for our full post-main sequence stellar population. We also compute occurrence rate values

of $0.35 \pm 0.05\%$ and $0.11_{-0.05}^{+0.06}\%$ for our sub-giant and early red giant sub populations respectively. Full details of how we define these sub-populations are provided in Section 2.2, but in brief we distinguish the two populations using a boundary of equal Evolutionary Equivalent Phase (EEP = 465) in $[T_{\text{eff}}, R_*]$ space (see Figure 1), such that our early red giant sub-population consists of stars which are more evolved than those in our sub-giant sub-population. The occurrence rate we measure for our early red giant sub-population is lower than the occurrence rate we measure for our sub-giant sub-population at a level of 3.1σ .

We plot our occurrence rate measurements as a function of planet period and radius for our full post-main sequence sample in Figure 7. The full occurrence rate results for the two sub-populations considered are plotted in Figure 8. We provide a summary of the giant planet occurrence rates we measure in this work in Table 2.

Our results show a clear decrease in the occurrence rate of short period giant planets for the more evolved host star sub-population. This suggests that the population of these giant planets decreases in number during these early stages of post-main sequence stellar evolution. From our occurrence rate results shown in Figure 8 we see that the occurrence rates for both sub-populations show a strong dependence with the orbital period of the planet. We compare the period dependence of the occurrence rates in Figure 9, where we can clearly see that the difference in occurrence rates between these two sub-populations is also dependent on the period of the planet. For moderate periods ($6 \leq P \leq 12$ days) we measure occurrence rates of $0.19 \pm 0.05\%$ for the sub-giant host star and $0.11_{-0.07}^{+0.14}\%$ for the more evolved early red giant host stars. The occurrence rates for these moderate periods are consistent between the two sub-populations within the uncertainties. However, for shorter orbital periods ($1 \leq P < 6$ days) the occurrence rate is significantly lower for the more evolved host stars. We measure occurrence rates of $0.17 \pm 0.02\%$ and $0.02_{-0.01}^{+0.02}\%$ for the sub-giant and early red giant sub-populations respectively finding an occurrence rate reduction for the more evolved early red giant sub-population at a level of 5.3σ .

Using a finer period spacing of 2 days shown in the bottom panel of Figure 9 we see that the largest measured occurrence rate differences are within the period range $2 \text{ days} \leq P < 6$ days, with consistent occurrence rate measurements for the shortest orbital periods, $P < 2$ days, for which we find an occurrence rate for our sub-giant sub-population of $0.003 \pm 0.002\%$ and an occurrence rate for our early red giant sub-population of $0.003 \pm 0.003\%$. However, we note that

Stellar Host Population	Period Range (days)	Planet Radius Range (R_{\oplus})	Occurrence Rate (%)	Comments
Full Post-Main Sequence	$1 \leq P \leq 12$	$8 \leq R_p \leq 22$	0.28 ± 0.04	Figure 7
	$1 \leq P < 6$	$8 \leq R_p \leq 22$	0.12 ± 0.02	
	$6 \leq P \leq 12$	$8 \leq R_p \leq 22$	0.17 ± 0.04	
	$1 \leq P \leq 10$	$8 \leq R_p \leq 22$	0.23 ± 0.03	*
Sub-Giant Sub-Population	$1 \leq P \leq 12$	$8 \leq R_p \leq 22$	0.35 ± 0.05	Figure 8
	$1 \leq P < 6$	$8 \leq R_p \leq 22$	0.17 ± 0.02	Figure 9
	$6 \leq P \leq 12$	$8 \leq R_p \leq 22$	0.19 ± 0.05	Figure 9
	$1 \leq P \leq 10$	$8 \leq R_p \leq 22$	$0.30^{+0.05}_{-0.04}$	Figure 10
	$1 \leq P \leq 10$	$9 \leq R_p \leq 22$	0.27 ± 0.04	† ; Figure 12
Early Red Giant Sub-Population	$1 \leq P \leq 12$	$8 \leq R_p \leq 22$	$0.11^{+0.06}_{-0.05}$	Figure 8
	$1 \leq P < 6$	$8 \leq R_p \leq 22$	$0.02^{+0.02}_{-0.01}$	Figure 9
	$6 \leq P \leq 12$	$8 \leq R_p \leq 22$	$0.11^{+0.14}_{-0.07}$	Figure 9
	$1 \leq P \leq 10$	$8 \leq R_p \leq 22$	$0.06^{+0.08}_{-0.03}$	Figure 10
	$1 \leq P \leq 10$	$9 \leq R_p \leq 22$	$0.06^{+0.09}_{-0.03}$	† ; Figure 12

* - Same parameter range as used for the comparison to previous main sequence studies in Figure 10

† - Direct comparison to [Beleznay & Kunimoto \(2022\)](#)

Table 2. Summary of the occurrence rates derived in this work for different planet parameter ranges and for different stellar populations. We provide occurrence rates for our full stellar sample as well as for our two sub-populations, which we distinguish using a boundary of equal Evolutionary Equivalent Phase (EEP = 465) in $[T_{\text{eff}}, R_*]$ space (see Section 2.2 and Figure 1 for more details).

the reduced number of planet detections for the early red giant host stars when considering more period bins in this way results in larger occurrence rate uncertainties. Therefore, at this stage we cannot say whether the agreement between our occurrence rate measurements for $P < 2$ days is a real astrophysical result or is simply due to the limited statistical significance of this measurements.

Our results clearly and significantly yield two key results about the population of short period giant planets with post-main sequence host stars. The first is that these occurrence rates are significantly lower for the more evolved early red giant host star sub-population, compared to the less evolved sub-giant host star sub-population. The second is that this occurrence rate reduction shows a strong period dependence, with shorter period planets showing a larger occurrence rate reduction.

7.2 Comparison to previous works

Only a few studies have previously measured planetary occurrence rates for post-main sequence host stars. Radial velocity surveys of giant stars have been performed (e.g. [Bowler et al. 2010](#); [Reffert et al. 2015](#)) although due to the low numbers of stars studied these surveys only yielded detections of planets on much wider orbits than those we study in this work. For example, [Bowler et al. \(2010\)](#) report the results of a survey of just 31 evolved stars and out of all their detected planets the lowest orbital semi-major axis is 0.68 AU. Whereas all our detected planets and candidates are at much closer separations of $a \leq 0.2$ AU. As these works probe a much different parameter space they do not provide a good comparison to our results, however we do note that this observed lack of planets at close orbital distances motivated suggestions that these planets had been destroyed by tidal interactions (e.g. [Schlaufman & Winn 2013](#)).

One study to which we can directly compare our results is that of [Grunblatt et al. \(2019\)](#) who used photometry from the *K2* mission to

measure an occurrence rate of short period giant planets ($3.5 \leq P \leq 10$ days; $R_p \geq 1 R_J$) around low-luminosity red giant branch stars ($R_* = 3 - 8 R_{\odot}$) of $0.49 \pm 0.28\%$. We note that this stellar sample likely consists of some stars of a similar evolution stage to the more evolved stars in our early red giant sample, and some stars which are more evolved than those we study in this work. Due to the large uncertainty of the [Grunblatt et al. \(2019\)](#) measurement, we find a difference between this value and the measured occurrence rate of $0.11^{+0.06}_{-0.05}\%$ for our early red giant sub-population of just 1.3σ . The [Grunblatt et al. \(2019\)](#) measurement is based on the detection of just three planets, with orbital periods of 8.4, 9.2, and 9.3 days. Therefore, their results also show evidence of a large reduction in occurrence rates for shorter orbital periods for evolved host stars, in qualitative agreement with our results.

Considering the null detection by [Grunblatt et al. \(2019\)](#) for giant planets with $3.5 \leq P \leq 8$ days we compute the occurrence rate for our early red giant sub-population for the period range $3.5 \leq P \leq 8$, measuring a value of $0.026^{+0.045}_{-0.016}\%$. The stellar sample surveyed by [Grunblatt et al. \(2019\)](#) consisted of 2476 stars. Therefore, considering our occurrence rate measurements we would expect just $0.64^{+1.11}_{-0.40}$ giant planets with $3.5 \leq P < 8$ days around these stars. Geometric transit probabilities for these systems will be on the order of 10-20%, and so the non-detection of any giant planets with $P \leq 8$ days by [Grunblatt et al. \(2019\)](#) is to be expected from our occurrence rate measurements. Therefore, our results for the population of giant planets with post-main sequence stars are not inconsistent with the previous findings from [Grunblatt et al. \(2019\)](#), but they are significantly more precise due to the much larger stellar sample made available to us by the TESS Full-Frame-Images.

At the end of their post-main sequence evolution the stars we studied in this work will become white dwarfs, and so it is interesting to contrast our results with the current investigations into the planetary populations around white dwarf stars. There have been a few studies

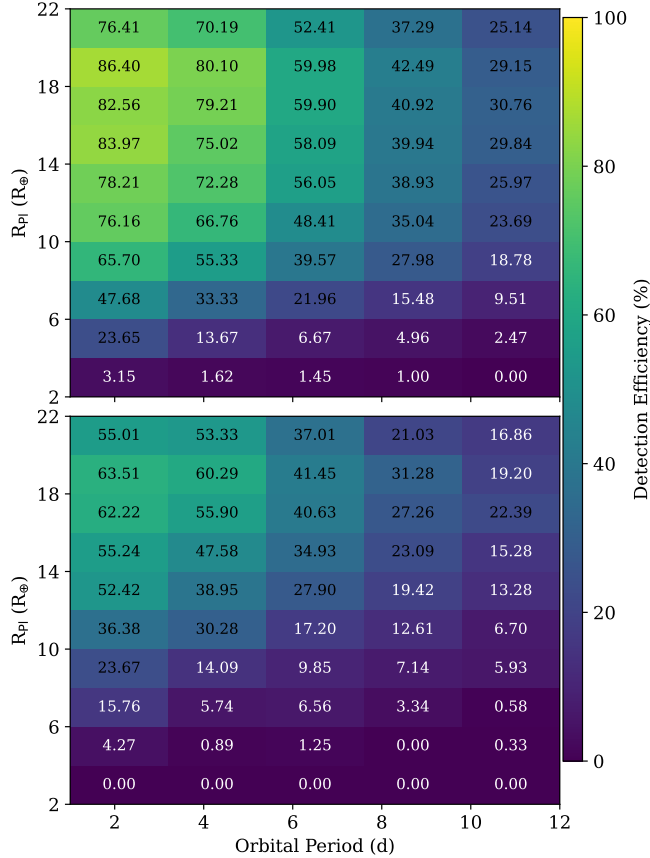


Figure 6. Detection efficiency of our full planet search and vetting pipeline for our two stellar sub-populations (see Section 2.2 and Figure 1). The detection efficiency for our sub-giant sub-population in the top panel and for our early red giant sub-population in the bottom panel. As for Figure 5 the colour of the grid cells gives the detection efficiency (%) for planets within the cell and the numbers in each box also give the percentage detection efficiency within each grid cell. The information shown on each panel is analogous to the right panel of Figure 5.

probing the occurrence of planets around white dwarfs (van Sluijs & Van Eylen 2018; Robert et al. 2024). Due to null detections of any planets van Sluijs & Van Eylen (2018) could only place an upper limit on the short period giant planet occurrence rate of $< 1.5\%$. The search of Robert et al. (2024) also did not yield the detection of any transiting giant-planet sized bodies. These null detections of any giant planets is in agreement with the rapid decrease in short period giant planet occurrence rates we observe in the post-main sequence stars we study. However there have been a few individual detections of planets orbiting white dwarfs (e.g. Gänsicke et al. 2019; Manser et al. 2019; Vanderburg et al. 2020). This suggests that a small number of planets may survive to the white dwarf stage of stellar evolution. Although these planets are expected to have resided on much wider orbits ($a > 1$ AU) during the stellar evolution stages we probe here (Vanderburg et al. 2020) and so again these works do not provide a direct contradiction of our results.

7.3 Comparison to the Main Sequence population

We now seek to compare our planet occurrence rates for giant planets orbiting evolved stars, to occurrence rates for similar planets that orbit stars which formed with similar properties but still reside on the main

sequence. A number of previous works have studied the occurrence rates of short period giant planets around solar-like main sequence stars. Using results from the *Kepler* mission (Borucki et al. 2010) for a sample of main sequence FGK type stars Howard et al. (2012) measured an occurrence rate for planets in the ranges $P < 10$ days and $8 \leq R_p \leq 32 R_\oplus$ of $0.4 \pm 0.1\%$ and Fressin et al. (2013) measured an occurrence rate of $0.43 \pm 0.05\%$ ($0.8 \leq P \leq 10$ days and $6 \leq R_p \leq 22 R_\oplus$). Combining the *Kepler* results for FGK main sequence stars with spectroscopic monitoring, Petigura et al. (2018) measured an occurrence rate of $0.57^{+0.14}_{-0.12}\%$, for planets with periods $1 \leq P \leq 10$ days and radii $8 \leq R_p \leq 24 R_\oplus$. Kunimoto & Matthews (2020) used the results from the complete *Kepler* DR25 release for main sequence FGK stars to measure an occurrence rate of $0.77^{+0.16}_{-0.14}\%$ ($P = 0.78 - 12.5$ days and $R_p = 8 - 16 R_J$). Using TESS photometry and considering giant planets with $0.9 \leq P \leq 10$ days and $0.8 \leq R_p \leq 2.5 R_J$ Zhou et al. (2019) measured an occurrence rate of $0.41 \pm 0.10\%$ for a sample of main sequence AFG stars ($0.8 < M_* \leq 2.3 M_\odot$). Expanding upon this work and also using TESS data, Beleznay & Kunimoto (2022) measured an occurrence rate of $0.33 \pm 0.04\%$ considering the same stellar and planetary ranges as Zhou et al. (2019). They also measure occurrence rates of $0.29 \pm 0.05\%$, $0.36 \pm 0.06\%$, and $0.55 \pm 0.14\%$ for A ($1.4 < M_* \leq 2.3 M_\odot$), F ($1.05 < M_* \leq 1.4 M_\odot$), and G ($0.8 < M_* \leq 1.05 M_\odot$) stars respectively. We summarise these results and compare them to our post-main sequence occurrence rate results in Figure 10.

All these previous works yield consistent results for the occurrence rate of short period giant planets around main sequence stars. In general these occurrence rates show agreement with our occurrence rate measurements for our sub-giant sub-population and are greater than our measured occurrence rates for our more evolved early red giant sub-population. However, all the main sequence occurrence rates consider slightly different stellar and planetary parameter ranges from each other. These parameters are all known to influence the measured occurrence rates and so a direct comparison to each previous study simultaneously cannot be robustly performed. Therefore, we select the results of Beleznay & Kunimoto (2022) for a detailed comparison to our results, primarily due to the fact that their results are derived from the largest stellar sample and they provide occurrence rate measurements for distinct stellar mass ranges. We do note that due to the overall agreement of the different main sequence occurrence rate results, comparing to the results of just Beleznay & Kunimoto (2022) is unlikely to impact our conclusions.

7.4 The occurrence rate reduction is not due to formation

The occurrence rate of short period giant planets is known to scale with the mass of the host star (Reffert et al. 2015; Kunimoto & Matthews 2020; Beleznay & Kunimoto 2022; Bryant et al. 2023). This has been linked to stars of different masses hosting protoplanetary discs of differing masses and lifetimes, which then influences the ability of a giant planet to form (e.g. Kennedy & Kenyon 2008; Alibert et al. 2011; Johnston et al. 2024). From our target selection criteria, we expect our sample to be dominated by stars in the mass range of $0.9 M_\odot \leq M_* \leq 1.4 M_\odot$, corresponding to stars which were F and G-dwarfs when on the main sequence. This is due to the $1.4 M_\odot$ stellar evolution track used to define the upper boundary of our stellar sample (see Figure 1), and the fact that lower mass stars are in general expected to have main sequence lifetimes longer than the age of the universe. In previous studies, there has been some debate over the stellar parameters for post-main sequence host stars (e.g. Lloyd 2011; Johnson et al. 2013; Schlaufman & Winn 2013). We note that for the stars in our sample the TIC either does not provide a mass or

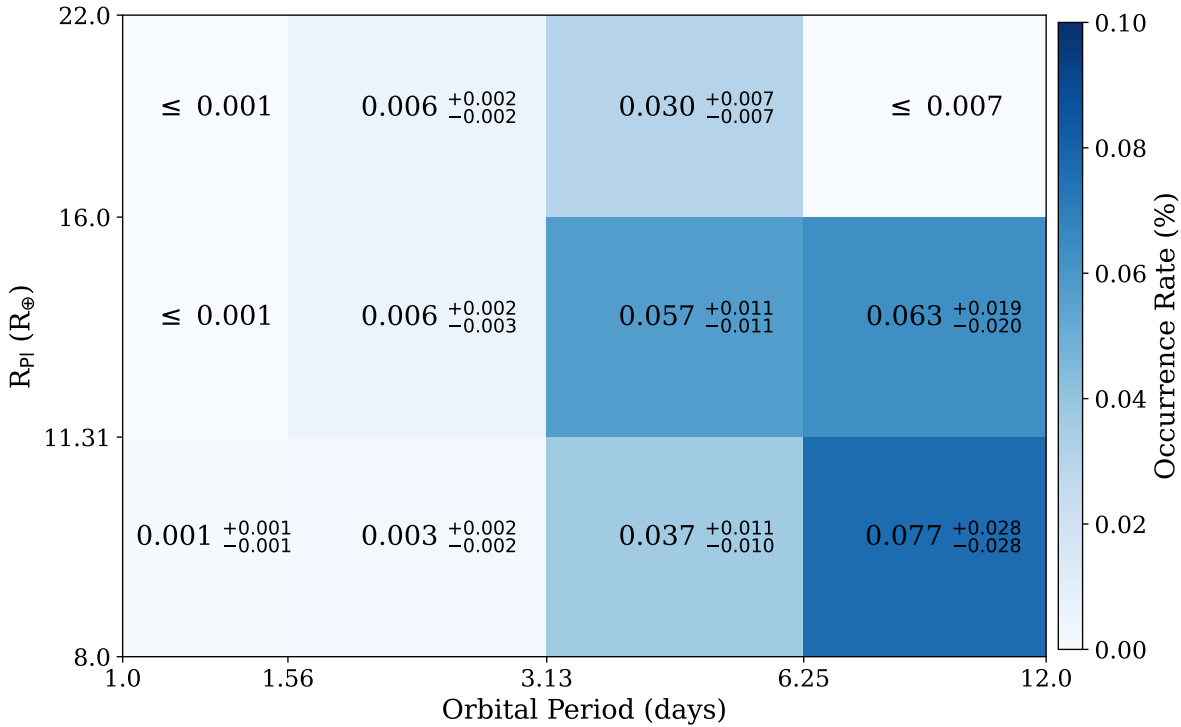


Figure 7. Occurrence rates measured in this study for post-main sequence host stars as a function of the planetary radius, R_p , and orbital period. The colour of each grid cell gives the occurrence rate in that grid cell, and the numbers quoted also provide a measure of the occurrence rate (%) within the corresponding grid cell. In the grid cells for which the measured occurrence rate is zero we report the 68th percentile upper limit.

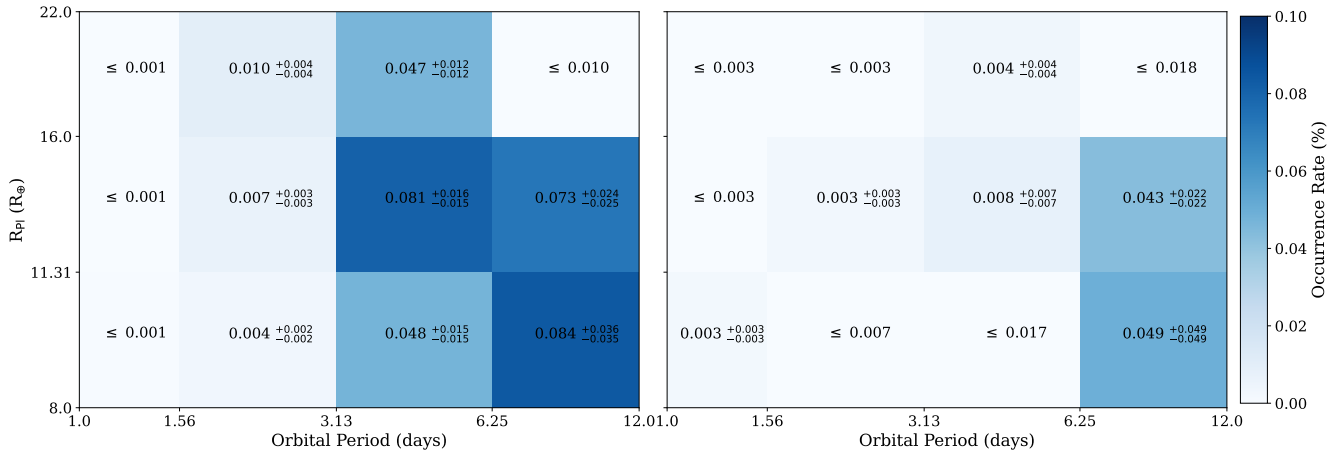


Figure 8. Occurrence rates measured for the two sub-populations considered in this study, with the sub-giant sub-population ($EEP < 465$) on the left and the more evolved, early red giant sub-population ($EEP \geq 465$) on the right. The colour scale and quoted numbers are as in Figure 7.

the quoted mass is unreliable (Stassun et al. 2019). Therefore, while we do expect our sample to be dominated by stars in the mass range equivalent to main sequence F and G stars, we look to obtain an independent assessment of the mass range covered by our sample.

To do this we use the Bayesian Stellar Algorithm (BASTA; Aguirre Børseth-Koch et al. 2022). BASTA uses stellar isochrones and evolution tracks, along with observable astrophysical stellar properties, to determine stellar parameters, and has been used widely to date for the characterisation of exoplanet host stars (e.g. Knudstrup et al. 2023; Persson et al. 2022; Osborne et al. 2024; Weeks et al. 2024). For such an analysis, it is important to have an estimate of the stellar metallicity, $[M/H]$. However, obtaining a robust metallicity for each

individual star in our sample requires careful observations and analysis which are beyond the scope of this work. Instead, we use the *Gaia* DR3 (Gaia Collaboration et al. 2023) results to obtain metallicity measurements for stars in our sample. Specifically we use the GSP-Spec metallicity values, which we calibrate following Recio-Blanco et al. (2023). We use these metallicities as input to BASTA, along with the stellar effective temperature as reported in the TIC, and the parallax, and *Gaia* G , G_{BP} , and G_{RP} magnitudes from *Gaia* DR3. The RA and dec coordinates for each star are also provided to obtain an estimate of the dust reddening.

Using BASTA we are then able to obtain a stellar mass estimate for 403,504 stars in our sample with an available GSP-Spec metallicity.

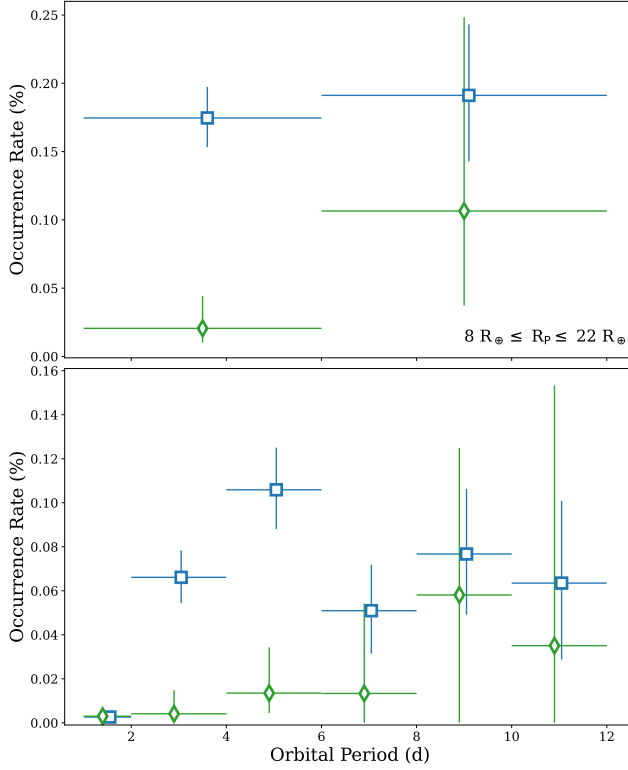


Figure 9. Period dependence of the giant planet occurrence rates we measure for the two post-main sequence sub-populations we consider (see Figure 1), plotting the occurrence rates for the sub-giant sub-population as the blue squares, and for the early red giant sub-population as the green diamonds.

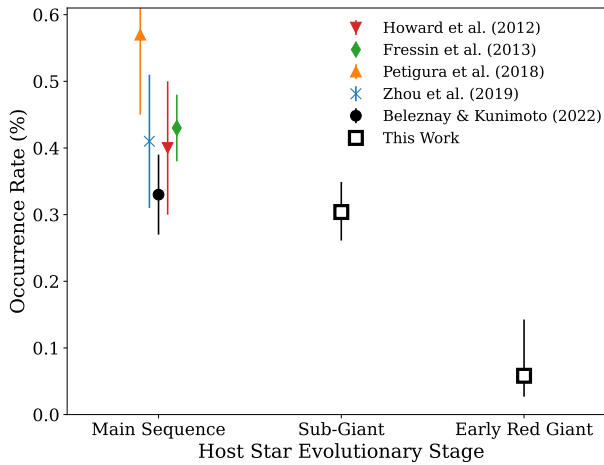


Figure 10. We compare our giant planet occurrence rate measurements (open squares) for the two sub-populations (see Figure 1) with the main sequence occurrence rate results from previous studies using results from *Kepler* and TESS. Our occurrence rate measurements shown in this plot were calculated using the following parameter ranges: $1 \leq P \leq 10$ days and $8 \leq R_p \leq 22 R_\oplus$. The period range was chosen to most closely match the period ranges used by the previous main sequence population studies (see Section 7.3 for more details on the parameter ranges considered by the other studies included here).

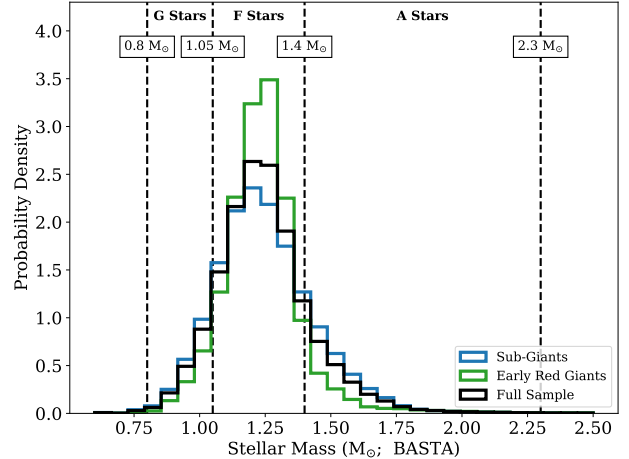


Figure 11. Mass probability density distribution for our post-main sequence sample. The vertical dashed lines denote the location of the stellar mass boundaries used by Beleznay & Kunimoto (2022) to distinguish main-sequence G-stars ($0.8 \leq M_* \leq 1.05 M_\odot$), F-stars ($1.05 \leq M_* \leq 1.4 M_\odot$), and A-stars ($1.4 \leq M_* \leq 2.3 M_\odot$)

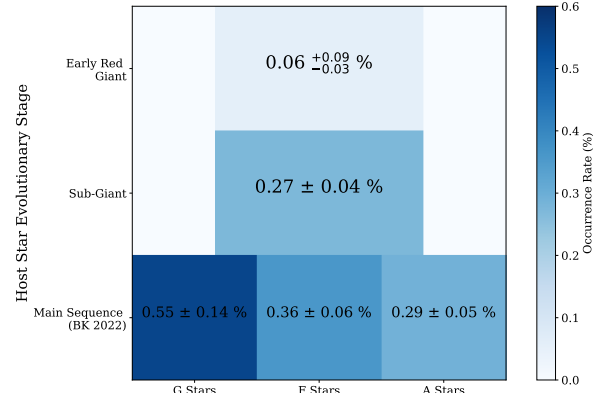


Figure 12. Comparison of the occurrence rate of giant planets as a function of the mass and evolutionary state of the host star sample. See the caption of Figure 11 for the corresponding mass used for G, F, and A stars.

We provide the BASTA mass distribution for our sample in Figure 11. The BASTA mass distribution results suggest that our post-main sequence stellar sample is indeed dominated by stars which were F-stars on the main sequence. The 95th percentile range for the BASTA results spans the mass range from $0.93 M_\odot$ to $1.67 M_\odot$, with 71.3% of the stars in our post-main sequence sample lying in the main sequence F-star mass range of $1.05 M_\odot \leq M_* \leq 1.4 M_\odot$ used by Beleznay & Kunimoto (2022). Following the mass ranges used by Beleznay & Kunimoto (2022), our post-main sequence stellar sample is most likely dominated by stars with a mass similar to main sequence F-stars, and also includes a few stars with a mass similar to main sequence early-G and late-A stars. We also note that we have no evidence for differing stellar mass distributions between our two sub-populations.

We compare our post-main sequence occurrence rates to the individual results for main sequence stars from Beleznay & Kunimoto (2022) in Figure 12. From this figure we can see that the occurrence rate we measure for our sub-giant population agrees with the main sequence F-star and A-star occurrence rates at a level of 1.25σ and 0.31σ respectively. For the early red giant sub-population, we see

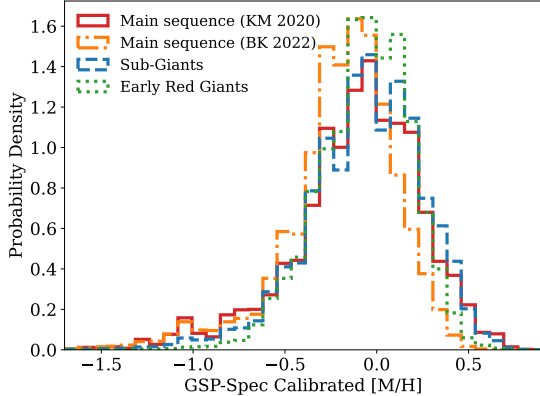


Figure 13. Probability density distributions of the GSP-Spec metallicities for our post-main sequence sample and our main sequence comparison samples. The metallicity distribution for our sub-giant sub-population is shown as the blue dashed line, and the distribution for our early red giant sub-population as the green dotted line. The GSP-Spec metallicity distributions we produce as representative comparisons for the [Kunimoto & Matthews \(2020\)](#) and [Beleznay & Kunimoto \(2022\)](#) main sequence samples are shown as the solid red line and dash-dotted orange line respectively.

that our measured occurrence rates are significantly lower than the main sequence occurrence rates, regardless of the stellar mass, at a level of 2.9σ , 2.8σ , and 2.2σ as compared to the main sequence G, F, and A-stars respectively.

The bulk metallicity of the host star can also impact the formation of giant planets ([Ida & Lin 2004](#); [Fischer & Valenti 2005](#); [Ercolano & Clarke 2010](#)). [Petigura et al. \(2018\)](#) studied the variation of planet occurrence rates with stellar metallicity. As a rough estimate from their results we might expect the occurrence rate to increase by a factor of two for a metallicity increase of 0.1 dex. We obtain GSP-Spec metallicity values, again calibrated following [Recio-Blanco et al. \(2023\)](#), for the stars included in the [Kunimoto & Matthews \(2020\)](#) main sequence sample. We note that there are available GSP-Spec metallicity values for only 5,297 of the 79,183 F- and G-stars they survey, primarily due to the intrinsic brightness of the *Kepler* stellar sample resulting in the majority of the stars being too faint for a GSP-Spec metallicity measurement. To obtain a representative comparison to the [Beleznay & Kunimoto \(2022\)](#) sample, we follow the selection criteria they provide in their Section 2.1, selecting stars from the TESS Candidate Target List (CTL; [Stassun et al. 2019](#)) with $T < 10.5$ mag, $0.8 M_{\odot} \leq M_{*} \leq 2.3 M_{\odot}$, and $\log g > 4.1$. This gives us a sample of 192,247 stars, 147,637 of which have an available GSP-Spec metallicity measurement. We compare the metallicity distributions of these stellar samples in Figure 13, from which we do not see large discrepancies between the metallicity distributions. Both our post-main sequence sub-populations display metallicity distributions that show good agreement with each other, as well as the [Kunimoto & Matthews \(2020\)](#) main-sequence sample. Fitting Gaussian models to the metallicity distributions we find mean values of -0.03 dex and -0.04 dex for our sub-giant and early red giant sub-populations respectively, as well as a value of -0.05 dex for the stars from the [Kunimoto & Matthews \(2020\)](#) sample.

The metallicity distributions for our sub-populations also show reasonable agreement with the [Beleznay & Kunimoto \(2022\)](#) comparison metallicity distribution, for which we find a mean value of -0.14 dex from fitting a Gaussian model, with our post-main se-

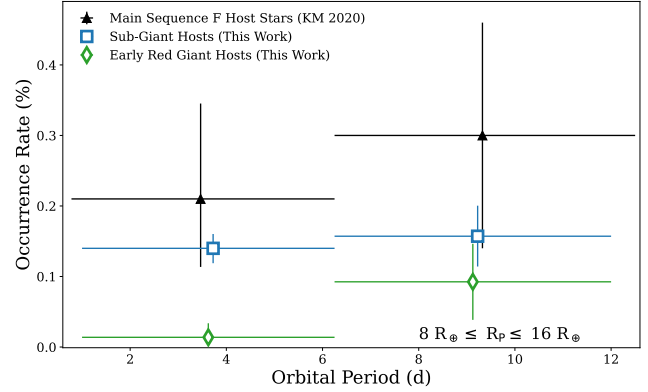


Figure 14. Variation of giant planet occurrence rates with orbital period for planets around evolved host stars (this work) and main sequence host stars ([Kunimoto & Matthews 2020](#)). For the evolved host stars we plot our results for our sub-giant sub-population as the blue squares and for our early red giant sub-population as the green diamonds. We compare to occurrence rates for main sequence F-stars (black triangles). The post-main sequence occurrence rates shown in these plots were computed using a planet radius range of $8 \leq R_p \leq 16 R_{\odot}$. This radius range is used for this plot to provide a like-for-like comparison to the [Kunimoto & Matthews \(2020\)](#) occurrence rates, which were computed using the same planet radius range (see Table 3 for details on these occurrence rate values).

quence samples showing a larger amount of super-solar metallicity stars. We therefore do not expect the stellar metallicities to be significantly biasing our occurrence rate measurements, and if anything we would expect our measured post-main sequence occurrence rates to be biased to slightly higher values as compared to the [Beleznay & Kunimoto \(2022\)](#) results. The true occurrence rate differences as a function of the stellar evolutionary state could therefore be slightly larger than we observe, although we note that as we are not comparing to the exact sample surveyed by [Beleznay & Kunimoto \(2022\)](#) we cannot make any strong conclusions.

From this analysis, we expect our post-main sequence stellar sample to be dominated by stars with masses similar to main sequence F-stars, and we see that our post-main sequence stars show similar bulk metallicity distributions to the main sequence stellar populations. Therefore, it is unlikely that the significant reduction we measure for the giant planet occurrence rates for our early red giant sub-population compared to the giant planet occurrence rates for main sequence stars is a result of reduced planet formation influenced by stellar mass or metallicity. Therefore, we have compelling evidence that the reduction in occurrence rates we observe for our post-main sequence stellar sample is the result of a process which occurs during the post-main sequence evolution of the host star, as a result of this evolution. We also have evidence that this process does not occur immediately at the onset of post-main sequence evolution, as our sub-giant population shows consistent giant planet occurrence rates with the main sequence F and A-stars, but instead occurs continuously throughout the early stages of the post-main sequence lifetime of the star. It is possible that this process is rapid orbital decay due to increased tidal interactions.

7.5 The reduction in giant planet occurrence is dependent on orbital period

We already saw that the occurrence rate difference between our two sub-populations is dependent on the planet orbital period (see Section 7.1). We would like to compare this effect to planets orbiting

Stellar Host Population	Period Range (days)	Occurrence Rate (%)	Reference
Main Sequence F-stars	$0.78 \leq P \leq 6.25$	$0.21^{+0.14}_{-0.10}$	Kunimoto & Matthews (2020)
Main Sequence F-stars	$6.25 < P \leq 12.5$	0.3 ± 0.16	Kunimoto & Matthews (2020)
Sub-Giant Stars	$1.0 \leq P \leq 6.25$	0.14 ± 0.02	<i>This Work</i>
Sub-Giant Stars	$6.25 < P \leq 12$	0.16 ± 0.04	<i>This Work</i>
Early Red Giant Stars	$1.0 \leq P \leq 6.25$	$0.014^{+0.020}_{-0.008}$	<i>This Work</i>
Early Red Giant Stars	$6.25 < P \leq 12$	0.09 ± 0.05	<i>This Work</i>

Table 3. Occurrence rates computed in this work for post-main sequence host stars the planet radius range $8 \leq R_p \leq 16 R_\oplus$ and for main sequence F-stars taken from [Kunimoto & Matthews \(2020\)](#). [Kunimoto & Matthews \(2020\)](#) define their F-star sample using the effective temperature range $6000 \leq T_{\text{eff}} < 7300$ K.

main sequence stars, however, [Beleznay & Kunimoto \(2022\)](#) do not provide their occurrence rate measurements as a function of orbital period. Instead, in order to compare the period dependence of our occurrence rates to the main sequence population, we use the results of [Kunimoto & Matthews \(2020\)](#). We make this comparison in Figure 14, comparing to the [Kunimoto & Matthews \(2020\)](#) results for main sequence F-stars, as these are likely to most closely match the stellar mass distribution of our stellar sample. We note that [Kunimoto & Matthews \(2020\)](#) consider planets in the range of $8 R_\oplus \leq R_p \leq 16 R_\oplus$. As such, we compute a new set of occurrence rate measurements using these radii limits for this comparison, to provide a more robust comparison. We provide these occurrence rates, along with those from [Kunimoto & Matthews \(2020\)](#) in Table 3.

We can see that the giant planet occurrence rate measured for our sub-giant sub-population is consistent with the main sequence F-stars for both short periods ($P \leq 6.25$ days) and moderate periods ($P > 6.25$ days), at levels of 0.69σ and 0.85σ respectively for the two period ranges. For our early red giant population, for the moderate planet period range we find the occurrence rate is consistent with the main sequence F-star occurrence rate at a level of 1.25σ . For the short period range we find a lower giant planet occurrence rate for the early red giant sub-population with a significance of 1.9σ . We note that the significance with which we can distinguish the main sequence and post-main sequence occurrence rates is primarily limited by the uncertainty on the main sequence occurrence rates from [Kunimoto & Matthews \(2020\)](#). Revisiting the period dependence of main sequence giant planet occurrence rates with the larger stellar sample available from the TESS mission, as compared to the *Kepler* mission, would enable these main sequence occurrence rates to be measured to a greater precision. This would enable the orbital period and stellar evolutionary stage at which the giant planet population begins to diminish, and the extent by which this occurs, to be determined to greater significance.

From the occurrence rates we measure in this work, and from the comparison of them to previous population studies for main sequence host stars, we have shown that the population of short period ($P \leq 12$ days) giant planets diminishes during the post-main sequence evolution of their host stars. We have also shown that the decrease in giant planet occurrence rates is larger for shorter orbital periods. This suggests that the giant planet population is being diminished by an evolutionary effect during the post-main sequence lifetime of the host stars, and it is very likely that tidal interactions between the planet and star are the source of this evolutionary influence.

7.6 Tidal Decay and Destruction

Tidal theories predict that interactions between stars and the planets orbiting them can lead to the planet's orbit shrinking and the planet spiralling in towards its host star (e.g. [Rasio et al. 1996](#)). The tidal interactions between stars and their close-in planets are believed to be dominated by two components: the equilibrium tide and the dynamical tide ([Zahn 1977, 1989, 2008](#)). While the exact mechanism dominating these interactions is unclear, the strength of these tidal interactions is also expected to depend strongly on the planet's semi-major axis with a smaller semi-major axis, and so a shorter orbital period, resulting in much stronger interactions and much faster orbital decay (e.g. [Goldreich & Soter 1966; Rasio et al. 1996](#)). Therefore, the fact that we observe a larger occurrence rate reduction for shorter orbital periods around more evolved stars is highly consistent with the picture in which these planet-star tidal interactions are sculpting the post-main sequence giant planet population.

The strength of these interactions is expected to increase during the post-main sequence evolution of the host stars. [Esseldeurs et al. \(2024\)](#) studied how tidal dissipation within stars changes throughout the evolution of the star, predicting an increase in the tidal dissipation for both the equilibrium and dynamical components from the beginning of the post-main sequence evolution phase. For stars with a convective envelope while on the main sequence, they predict a gradual increase in the in the tidal dissipation, while for stars with a radiative envelope on the main sequence the predicted tidal dissipation increase is instantaneous. [Barker \(2020\)](#) also investigated the expected variation in tidal dissipation throughout the evolution of stars. They find that dynamical tides due to the dissipation of internal waves may become highly, if briefly, efficient as the star evolves off the main sequence. Their results also predict the dissipation of equilibrium tides to be impactful for evolved stars and negligible during the main sequence.

[Weinberg et al. \(2024\)](#) also study the predicted tidal dissipation in sub-giant stars and the orbital decay time for planets in orbit around them. For stars with $M_* \leq 1.0 M_\odot$ they find a slight increase in the orbital decay time as the star evolves. For more massive stars ($M_* \geq 1.2 M_\odot$) they predict minimal tidal decay while the stars are on the main sequence, but they find that the orbital decay time decreases significantly as the star evolves off the main sequence. On the sub-giant branch, [Weinberg et al. \(2024\)](#) find that the orbital decay time can be faster than 10 Myr around these higher mass stars for the shortest orbital periods, $P \leq 2$ days. Even for slightly longer orbital periods, $P \leq 4$ days, they find orbital decay timescales on the order of 100 Myr for the older sub-giant models they consider. [Weinberg et al. \(2024\)](#) note that this timescale is comparable to the evolutionary timescale of these sub-giant stars.

From our results we find that the short period giant planet occurrence rates in general are consistent between the main sequence

stellar population and our sub-giant sub-population, which consists of stars that have only just begun their post-main sequence evolution. We also find significantly reduced giant planet occurrence rates for our sub-population of more evolved early red giant host stars, noting that this more evolved stellar population still represents an early stage relative to the full post-main sequence evolution of these stars. Therefore, our results are in agreement with these theoretical predictions that these tidal interactions increase in strength as the stars evolve off of the main sequence, with rapid tidal decay occurring during the early stages of the post-main sequence lifetime of these stars.

Our results therefore provide strong evidence that the population of short period giant planets is heavily impacted by the post-main sequence evolution of their host stars. The increased strength of the planet-star tidal interactions, as a result of the changing stellar structure during the early stages of post-main sequence evolution, is the most likely driving force impacting the giant planet population.

Recent works have claimed that the occurrence rate of short period giant planets with main sequence host stars decreases with increasing stellar age (Chen et al. 2023; Miyazaki & Masuda 2023). These works have suggested that such a decrease may be due to these tidal effects having an impact on the giant planet population even during the main sequence lifetime of their host stars (Chen et al. 2023; Miyazaki & Masuda 2023).

Moreover, while we are limited by the small number of candidate planets at these short orbital periods, we do not see a difference between the measured giant planet occurrence rates for $P \leq 2$ days for our sub-giant and early red giant sub-populations (see Figure 9 and Section 7.1). We note that we cannot rule out this simply being a result of the limited statistical significance of our results due to a lack of detected planets at these very short orbital periods. However if this is a real astrophysical feature of the population then it would be in keeping with the prediction from Weinberg et al. (2024) that planets at these short orbital periods exhibit very short tidal decay timescales around post-main sequence stars, and so full orbital decay is to be expected before their host stars evolve to the bottom of the red giant branch.

7.7 Studying post-main sequence population demographics with our detected planet sample

Beyond the occurrence rates we measure in this work, the sample of 118 giant planets and planet candidates with post-main sequence host stars we detected using our homogeneous planet search and vetting pipeline represents a statistically unbiased planet population with which to study the demographics of the post-main sequence planet population. For example, it has previously been suggested that the population of planets with evolved host stars may reside on more eccentric orbits than planets with main sequence host stars, potentially as a result of the tidal interactions between the planets and their host stars (e.g. Villaver et al. 2014; Grunblatt et al. 2018). In addition, it has been predicted that the increased irradiation of these planets due to the increase in radius and luminosity of their evolving host stars can cause these planets to undergo a level of re-inflation (e.g. Grunblatt et al. 2017; Thorngren et al. 2021). Moreover, recent obliquity measurements for hot Jupiters orbiting sub-giants suggest that the tidal interactions in these systems may also lead to highly efficient damping of the orbital obliquity of these systems (Saunders et al. 2024).

However, the specific study of these demographics is beyond the scope of this paper, primarily as further spectroscopic observations of our planet candidates will be required. This is because having an accurate measure of the planet mass is crucial for understanding the

tidal interactions as the strength of them is predicted by tidal theory to depend on the planet to star mass ratio, M_p/M_* , with higher mass ratios resulting in stronger tidal interactions (Ogilvie 2014; Patra et al. 2020). The planet mass is also a key component for understanding the level of planet radius inflation observed (Sestovic et al. 2018). Fortunately, as our candidate planets have relatively bright host stars ($T \leq 12$ mag) and are likely to exhibit large radial velocity semi-amplitudes on the order of tens or even hundreds m s^{-1} the measurement of their masses should be easily within the capabilities of existing spectrographs, such as HARPS (Mayor et al. 2003) and HARPS-N (Cosentino et al. 2012). Precisely monitoring the radial velocity variation for these stars will also yield a measurement of the orbital eccentricity of these systems.

Through these radial velocity observations we will also be able to refine our occurrence rate measurements, which are calculated using false positive probability (FPP) estimates computed using the TRICERATOPS software package (Giacalone & Dressing 2020). While, these FPP estimates are a key aspect of measuring planet occurrence rates and TRICERATOPS has been widely used for that purpose (e.g. Bryant et al. 2023; Vach et al. 2024; Giacalone & Dressing 2025), radial velocity follow up observations would enable us to confirm or reject the planet candidates in our sample as bona-fide planets, thus refining our knowledge of the overall population.

Finally, of particular interest from the 82 new candidates and TOIs we detect using our pipeline are eleven with short orbital periods $P \leq 2$ days, shorter than any currently confirmed giant planets around sub-giant and red giant stars. As shorter period planets are expected to exhibit more rapid tidal decay (e.g. Rasio et al. 1996) then if these candidates are confirmed as real planets they would therefore become key puzzle pieces for understanding how post-main sequence stars impact their close-in giant planets.

8 CONCLUSIONS

We conduct a systematic transit search for giant planets ($8 R_\oplus \leq R_p \leq 22 R_\oplus$) on short orbital periods ($1 \leq P \leq 12$ days) around a sample of 456,941 post-main sequence stars, using TESS Full-Frame-Image data produced by the QLP pipeline. From this search we detected a sample of 118 giant planets and planet candidates, and a further twelve planets and candidates with smaller radii, $R_p < 8 R_\oplus$. Using injection-recovery simulations to quantify the detection efficiency of our planet search and candidate vetting pipeline we measure the short period giant planet occurrence rate of this population, deriving a value of $0.28 \pm 0.04\%$ across our full post-main sequence stellar sample.

We also divide our stellar sample using a boundary of equal Equivalent Evolutionary Phase, $\text{EEP} = 465$ (Choi et al. 2016) into two stellar sub-populations: our sub-giant sub-population, which consists of stars in the earliest stages of post-main sequence evolution, and our early red giant sub-population of more evolved stars (see Section 2.2 and Figure 1). We measure occurrence rates for our two sub-populations, finding values of $0.35 \pm 0.05\%$ for our sub-giant sub-population and $0.11^{+0.06}_{-0.05}\%$ for our early red giant sub-population, finding a significant decrease in giant planet occurrence rates for more evolved stars. We also show that the decrease in occurrence rate is dependent on the planet orbital period with a larger occurrence rate difference observed for shorter period planets.

Comparing our results with previous occurrence rate measurements for main sequence host stars (Howard et al. 2012; Fressin et al. 2013; Petigura et al. 2018; Zhou et al. 2019; Kunimoto & Matthews 2020; Beleznay & Kunimoto 2022), we again find a significant de-

crease for our early red giant sub-population as compared to the main sequence, again with a greater occurrence rate decrease for shorter period planets. For our sub-giant sample we find our measured giant planet occurrence rate shows agreement with the main sequence planet population. By considering the mass and metallicity distributions of the main sequence and post-main sequence stellar samples we show that a differing level of giant planet formation due to variations in these parameters is unlikely to be the cause of the occurrence rate trends we observe.

We conclude that the reduction in giant planet occurrence rates for more evolved stars we observe is due to these planets being impacted by the post-main sequence evolution of their host stars. Due to the period dependence observed for the occurrence rate decrease we conclude that the dominant impact is most likely rapid tidal decay of the planets' orbits due to the increasing strength of the planet-star tidal interactions as the host stars evolve (e.g. Rasio et al. 1996; Barker 2020; Esseldeurs et al. 2024; Weinberg et al. 2024).

Our homogeneously detected sample of planets and planet candidates with post-main sequence host stars also represents a quality resource with which to study wider demographics of the post-main sequence, such as giant planet re-inflation (e.g. Grunblatt et al. 2017; Thorngren et al. 2021) or the orbital eccentricity distribution of these systems (e.g. Villaver et al. 2014; Grunblatt et al. 2018). Accurate and precise individual mass measurements for all our planet candidates and host stars are required before studying these aspects of the post-main sequence giant planet population. Observing the host stars spectroscopically, for example with spectrographs such as HARPS, will provide the spectra necessary to better understand the nature of the stars and determine the mass of the orbiting companions. Such spectroscopic observations would also refine our occurrence rate measurements through the confirmation of our planet candidates and would also enable us to better understand the tidal mechanisms at play in these systems.

One further limit to our ability to constrain the impact of post-main sequence evolution on the giant planet population is our knowledge of the main sequence giant planet population and how this varies with orbital period. Revisiting these occurrence rates, and how they vary with stellar mass and orbital period, with the full extent of the TESS Full-Frame-Image observations will enable us to see any differences between the main-sequence and post-main sequence more clearly.

Obtaining a better characterisation of the stars surveyed would also improve our understanding of the impact of post-main sequence evolution on the giant planet population. An improved understanding of the evolutionary stage of each of the stars in our sample would allow us to better constrain how the population varies during this evolution. Obtaining better constraints of the mass and metallicities of the stars in our sample as well as the stars in any main sequence comparison sample would also enable us predict the impact of these on the giant planet occurrence rates, thereby allowing us to better disentangle these formation effects from the evolutionary effects.

The PLATO mission (Rauer et al. 2014) can play a large role in the future in understanding the post-main sequence planet population. PLATO will deliver much higher precision photometry than TESS which will enable us to detect planets and measure occurrence rates for more evolved larger radius planets on the red giant branch. PLATO will also enable us to accurately characterise these stars through asteroseismology, providing much better constraints on the masses and evolution states for all the stars studied.

ACKNOWLEDGEMENTS

We are grateful to Angharad Weeks for useful discussions and support around the use of BASTA to obtain stellar mass estimates. The contributions at the Mullard Space Science Laboratory by E.M.B. have been supported by STFC through the consolidated grant ST/W001136/1. V.V.E. has been supported by UK's Science & Technology Facilities Council through the STFC grants ST/W001136/1 and ST/S000216/1. This research has made use of the NASA Exoplanet Archive, which is operated by the California Institute of Technology, under contract with the National Aeronautics and Space Administration under the Exoplanet Exploration Program. This paper includes data collected by the TESS mission, which are publicly available from the Mikulski Archive for Space Telescopes (MAST). Funding for the TESS mission is provided by NASA's Science Mission Directorate. We acknowledge the use of public TOI Release data from pipelines at the TESS Science Office and at the TESS Science Processing Operations Center.

DATA AVAILABILITY

The TESS Quick Look Pipeline light curves used in this work are all publicly available as a MAST High Level Science Product. They can be accessed from <https://archive.stsci.edu/hlsp/qlp>.

REFERENCES

Aguirre Børseth-Koch V., et al., 2022, *MNRAS*, 509, 4344
 Akana Murphy J. M., et al., 2023, *AJ*, 166, 153
 Alibert Y., Mordasini C., Benz W., 2011, *A&A*, 526, A63
 Anderson D. R., et al., 2015, *A&A*, 575, A61
 Bakos G. Á., et al., 2009, *ApJ*, 707, 446
 Barclay T., Endl M., Huber D., Foreman-Mackey D., Cochran W. D., MacQueen P. J., Rowe J. F., Quintana E. V., 2015, *ApJ*, 800, 46
 Barker A. J., 2020, *Monthly Notices of the Royal Astronomical Society*, 498, 2270
 Barker A. J., Ogilvie G. I., 2010, *MNRAS*, 404, 1849
 Bayliss D. D. R., Sackett P. D., 2011, *ApJ*, 743, 103
 Beatty T. G., et al., 2012, *ApJ*, 756, L39
 Beleznay M., Kunimoto M., 2022, *MNRAS*, 516, 75
 Berger T. A., Huber D., Gaidos E., van Saders J. L., 2018, *ApJ*, 866, 99
 Borucki W. J., et al., 2010, *Science*, 327, 977
 Bowler B. P., et al., 2010, *ApJ*, 709, 396
 Brahm R., et al., 2020, *AJ*, 160, 235
 Bryant E. M., et al., 2020, *MNRAS*, 499, 3139
 Bryant E. M., Bayliss D., Van Eylen V., 2023, *MNRAS*, 521, 3663
 Caldwell D. A., et al., 2020, *Research Notes of the American Astronomical Society*, 4, 201
 Chen D.-C., et al., 2023, *Proceedings of the National Academy of Science*, 120, e2304179120
 Choi J., Dotter A., Conroy C., Cantiello M., Paxton B., Johnson B. D., 2016, *The Astrophysical Journal*, 823, 102
 Chontos A., et al., 2019, *AJ*, 157, 192
 Cooke B. F., et al., 2020, *AJ*, 159, 255
 Cosentino R., et al., 2012, in McLean I. S., Ramsay S. K., Takami H., eds, Society of Photo-Optical Instrumentation Engineers (SPIE) Conference Series Vol. 8446, Ground-based and Airborne Instrumentation for Astronomy IV. p. 84461V. doi:10.1117/12.925738
 Dawson R. I., Johnson J. A., 2012, *ApJ*, 756, 122
 Delrez L., et al., 2014, *A&A*, 563, A143
 Dotter A., 2016, *The Astrophysical Journal Supplement Series*, 222, 8
 Enoch B., et al., 2011, *AJ*, 142, 86
 Ercolano B., Clarke C. J., 2010, *Monthly Notices of the Royal Astronomical Society*, 402, 2735

Esseldeurs M., Mathis S., Decin L., 2024, *A&A*, **690**, A266

Fischer D. A., Valenti J., 2005, *ApJ*, **622**, 1102

Foreman-Mackey D., Hogg D. W., Lang D., Goodman J., 2013, *PASP*, **125**, 306

Fressin F., et al., 2013, *The Astrophysical Journal*, 766, 81

Gaia Collaboration et al., 2018, *A&A*, **616**, A1

Gaia Collaboration et al., 2023, *A&A*, **674**, A1

Gan T., et al., 2023, *AJ*, **165**, 17

Gänsicke B. T., Schreiber M. R., Toloza O., Gentile Fusillo N. P., Koester D., Manser C. J., 2019, *Nature*, **576**, 61

Giacalone S., Dressing C. D., 2020, triceratops: Candidate exoplanet rating tool, Astrophysics Source Code Library, record ascl:2002.004

Giacalone S., Dressing C. D., 2025, *AJ*, **169**, 45

Giacalone S., et al., 2021, *AJ*, **161**, 24

Gillon M., et al., 2013, *A&A*, **552**, A82

Goldreich P., Soter S., 1966, *Icarus*, **5**, 375

Grunblatt S. K., et al., 2017, *AJ*, **154**, 254

Grunblatt S. K., et al., 2018, *The Astrophysical Journal Letters*, 861, L5

Grunblatt S. K., Huber D., Gaidos E., Hon M., Zinn J. C., Stello D., 2019, *AJ*, **158**, 227

Grunblatt S. K., et al., 2022, *AJ*, **163**, 120

Guerrero N. M., et al., 2021, *ApJS*, **254**, 39

Hadjigeorgiou A., Armstrong D. J., 2024, *MNRAS*, **527**, 4018

Hartman J. D., et al., 2015, *AJ*, **150**, 168

Hartman J. D., et al., 2019, *AJ*, **157**, 55

Hellier C., et al., 2012, *MNRAS*, **426**, 739

Hellier C., et al., 2014, *MNRAS*, **440**, 1982

Hellier C., et al., 2019, *MNRAS*, **482**, 1379

Hippke M., David T. J., Mulders G. D., Heller R., 2019, *The Astronomical Journal*, 158, 143

Howard A. W., et al., 2012, *ApJS*, **201**, 15

Howell S. B., et al., 2014, *Publications of the Astronomical Society of the Pacific*, **126**, 398

Huang C. X., et al., 2020, *Research Notes of the American Astronomical Society*, **4**, 206

Huber D., 2019, evolstate: Assign simple evolutionary states to stars, Astrophysics Source Code Library, record ascl:1905.003

Ida S., Lin D. N. C., 2004, *The Astrophysical Journal*, 616, 567

Jackson B., Greenberg R., Barnes R., 2008, *ApJ*, **678**, 1396

Johnson J. A., Aller K. M., Howard A. W., Crepp J. R., 2010, *PASP*, **122**, 905

Johnson J. A., Morton T. D., Wright J. T., 2013, *ApJ*, **763**, 53

Johnson M. C., et al., 2018, *MNRAS*, **481**, 596

Johnston H. F., Panić O., Liu B., 2024, *MNRAS*, **527**, 2303

Kabáth P., et al., 2022, *MNRAS*, **513**, 5955

Kennedy G. M., Kenyon S. J., 2008, *ApJ*, **673**, 502

Kipping D. M., 2013, *MNRAS*, **435**, 2152

Knudstrup E., et al., 2022, *A&A*, **667**, A22

Knudstrup E., et al., 2023, *MNRAS*, **519**, 5637

Kossakowski D., et al., 2019, *MNRAS*, **490**, 1094

Kovács G., Zucker S., Mazeh T., 2002, *A&A*, **391**, 369

Kovács G., et al., 2007, *ApJ*, **670**, L41

Kreidberg L., 2015, *PASP*, **127**, 1161

Kunimoto M., Matthews J. M., 2020, *AJ*, **159**, 248

Kunimoto M., et al., 2021, *Research Notes of the American Astronomical Society*, **5**, 234

Kunimoto M., Tey E., Fong W., Hesse K., Shporer A., Fausnaugh M., Vander spek R., Ricker G., 2022, *Research Notes of the American Astronomical Society*, **6**, 236

Lam K. W. F., et al., 2017, *A&A*, **599**, A3

Lightkurve Collaboration et al., 2018, Lightkurve: Kepler and TESS time series analysis in Python, Astrophysics Source Code Library, record ascl:1812.013

Lillo-Box J., et al., 2014, *A&A*, **562**, A109

Lloyd J. P., 2011, *ApJ*, **739**, L49

Lloyd J. P., 2013, *ApJ*, **774**, L2

Lomb N. R., 1976, *Ap&SS*, **39**, 447

Mandushev G., et al., 2007, *ApJ*, **667**, L195

Manser C. J., et al., 2019, *Science*, **364**, 66

Mayor M., et al., 2003, *The Messenger*, **114**, 20

McCullough P. R., et al., 2008, *arXiv e-prints*, p. arXiv:0805.2921

Miyazaki S., Masuda K., 2023, *AJ*, **166**, 209

Montalto M., et al., 2020, *MNRAS*, **498**, 1726

Montalto M., et al., 2022, *MNRAS*, **509**, 2908

Moutou C., et al., 2021, *A&A*, **653**, A147

Mustill A. J., Villaver E., 2012, *ApJ*, **761**, 121

Neath A. A., Cavanaugh J. E., 2012, *WIREs Computational Statistics*, **4**, 199

Neveu-VanMalle M., et al., 2014, *A&A*, **572**, A49

Newville M., Stensitzki T., Allen D. B., Rawlik M., Ingargiola A., Nelson A., 2016, lmfit: Non-Linear Least-Square Minimization and Curve-Fitting for Python, Astrophysics Source Code Library, record ascl:1606.014

Nielsen L. D., et al., 2019, *MNRAS*, **489**, 2478

Ogilvie G. I., 2014, *ARA&A*, **52**, 171

Osborne H. L. M., et al., 2024, *MNRAS*, **527**, 11138

Patra K. C., et al., 2020, *The Astronomical Journal*, 159, 150

Pereira F., et al., 2024, *MNRAS*, **527**, 6332

Persson C. M., et al., 2022, *A&A*, **666**, A184

Petigura E. A., et al., 2018, *The Astronomical Journal*, 155, 89

Polanski A. S., et al., 2024, *ApJS*, **272**, 32

Rasio F. A., Tout C. A., Lubow S. H., Livio M., 1996, *ApJ*, **470**, 1187

Rauer H., et al., 2014, *Experimental Astronomy*, **38**, 249

Recio-Blanco A., et al., 2023, *A&A*, **674**, A29

Reffert S., Bergmann C., Quirrenbach A., Trifonov T., Künstler A., 2015, *A&A*, **574**, A116

Ricker G. R., et al., 2015, *Journal of Astronomical Telescopes, Instruments, and Systems*, **1**, 014003

Robert A., et al., 2024, *MNRAS*, **533**, 1756

Rodriguez J. E., et al., 2023, *MNRAS*, **521**, 2765

Saunders N., et al., 2022, *AJ*, **163**, 53

Saunders N., et al., 2024, *AJ*, **168**, 81

Scargle J. D., 1982, *ApJ*, **263**, 835

Schlaufman K. C., Winn J. N., 2013, *ApJ*, **772**, 143

Schulte J., et al., 2024, *AJ*, **168**, 32

Serrano Bell J., et al., 2024, *A&A*, **684**, A6

Sestovic M., Demory B.-O., Queloz D., 2018, *A&A*, **616**, A76

Sha L., et al., 2021, *AJ*, **161**, 82

Smalley B., et al., 2012, *A&A*, **547**, A61

Smith A. M. S., et al., 2013, *A&A*, **552**, A120

Stassun K. G., et al., 2019, *AJ*, **158**, 138

Thorngren D. P., Fortney J. J., Lopez E. D., Berger T. A., Huber D., 2021, *The Astrophysical Journal Letters*, 909, L16

Vach S., et al., 2024, *AJ*, **167**, 210

Van Eylen V., Albrecht S., 2015, *ApJ*, **808**, 126

Van Eylen V., et al., 2016, *AJ*, **152**, 143

Van Eylen V., et al., 2018, *MNRAS*, **478**, 4866

Vanderburg A., et al., 2020, *Nature*, **585**, 363

Vanderspek R., Doty J., Fausnaugh M., et al., 2018, TESS Instrument Handbook v0. 1, TESS Science Office

Veras D., 2016, *Royal Society Open Science*, **3**, 150571

Villaver E., Livio M., 2009, *ApJ*, **705**, L81

Villaver E., Livio M., Mustill A. J., Siess L., 2014, *The Astrophysical Journal*, 794, 3

Weeks A., et al., 2024, *arXiv e-prints*, p. arXiv:2411.17358

Weinberg N. N., Davachi N., Essick R., Yu H., Arras P., Belland B., 2024, *ApJ*, **960**, 50

West R. G., et al., 2016, *A&A*, **585**, A126

Yee S. W., et al., 2020, *ApJ*, **888**, L5

Yee S. W., et al., 2022, *AJ*, **164**, 70

Yee S. W., et al., 2023, *ApJS*, **265**, 1

Zahn J. P., 1977, *A&A*, **57**, 383

Zahn J. P., 1989, *A&A*, **220**, 112

Zahn J. P., 2008, in Goupil M. J., Zahn J. P., eds, EAS Publications Series Vol. 29, EAS Publications Series. pp 67–90 (arXiv:0807.4870), doi:10.1051/eas:0829002

Zhou G., et al., 2019, *The Astronomical Journal*, 158, 141

da Silva R., et al., 2006, *A&A*, **446**, 717

do Nascimento J. D., da Costa J. S., Castro M., 2012, *A&A*, **548**, L1

APPENDIX A: PLANET CANDIDATE TABLES

Table A1: Stellar and planetary properties for the new planet candidates we detect with our planet search pipeline and their host stars

TIC	T (mag)	R_* (R_\odot ; TIC)	T_{eff} (K; TIC)	Sub-Population*	P (days)	$T_C - 2457000$	R_P/R_*	$R_P(R_\oplus)$	a/R_*	i (degrees)	b
14230289	11.61	1.93 ± 0.10	6276 ± 129	SG	2.41097 ± 0.00044	2449.5805 ± 0.0026	0.073 ± 0.1674	15.3 ± 35.2	9.1 ± 3.3	65.5 ± 3.4	0.72 ± 0.41
21355897	10.28	2.74 ± 0.14	6262 ± 134	SG	5.3424 ± 0.0107	2363.4833 ± 0.017	0.0551 ± 0.0095	16.5 ± 2.8	4.82 ± 0.88	84.7 ± 3.8	0.46 ± 0.4
4832914	11.95	1.79 ± 0.10	6220 ± 126	SG	4.31651 ± 0.00047	2338.3026 ± 0.0016	0.0945 ± 0.0019	18.5 ± 2.1	1.088 ± 0.12	87.9 ± 1.5	0.4 ± 0.26
64329653	11.39	1.73 ± 0.09	5802 ± 125	SG	4.3976 ± 0.0029	2231.2925 ± 0.0058	0.071 ± 0.0076	13.36 ± 1.42	11.6 ± 2.2	87.3 ± 1.9	0.55 ± 0.28
20265363	11.28	2.07 ± 0.15	6232 ± 96	SG	4.24748 ± 0.00062	2202.727 ± 0.0017	0.0774 ± 0.0018	17.51 ± 0.43	7.41 ± 0.35	87.7 ± 1.6	0.5 ± 0.22
241470435	11.66	2.28 ± 0.13	5827 ± 118	SG	5.4997 ± 0.0028	2334.6001 ± 0.0074	0.0513 ± 0.004	12.8 ± 2.6	7.8 ± 1.3	85.7 ± 3.1	0.58 ± 0.32
241630802	11.84	1.63 ± 0.09	5937 ± 128	SG	8.1552 ± 0.003	2122.7835 ± 0.0041	0.0581 ± 0.0034	10.3 ± 0.61	19.6 ± 2.0	88.8 ± 0.84	0.42 ± 0.29
25566000	11.65	2.59 ± 0.18	5811 ± 129	SG	7.4225 ± 0.004	2504.024 ± 0.017	0.0388 ± 0.0046	10.97 ± 1.3	6.4 ± 1.4	85.0 ± 3.6	0.27 ± 0.31
280514270	11.36	2.34 ± 0.12	6045 ± 136	SG	1.24525 ± 0.0003	2309.4702 ± 0.0097	0.0338 ± 0.0045	8.6 ± 1.6	3.1 ± 1.2	78.1 ± 9.0	0.67 ± 0.39
314729618	11.80	3.05 ± 0.15	6244 ± 133	SG	1.42823 ± 0.00065	2335.7128 ± 0.0062	0.0508 ± 0.0042	16.9 ± 1.4	3.12 ± 0.42	81.7 ± 5.9	0.46 ± 0.31
331673033	11.88	1.34 ± 0.07	5473 ± 126	SG	2.4665 ± 0.0012	2336.4933 ± 0.0117	0.0576 ± 0.0082	8.42 ± 1.2	4.89 ± 0.93	84.2 ± 4.2	0.5 ± 0.36
38055340	11.41	1.69 ± 0.08	6143 ± 133	SG	6.32978 ± 0.00063	2312.4576 ± 0.0028	0.1203 ± 0.0059	22.23 ± 0.72	7.16 ± 0.49	83.5 ± 0.65	0.829 ± 0.023
38323315	11.41	2.76 ± 0.14	5912 ± 130	SG	6.1594 ± 0.0015	2308.2795 ± 0.0086	0.0444 ± 0.0057	13.4 ± 1.6	9.8 ± 3.3	86.1 ± 2.9	0.68 ± 0.33
397510904	11.64	2.61 ± 0.14	6151 ± 514	SG	$1.616151 \pm 8.2e-05$	2391.1715 ± 0.011	0.034 ± 0.0483	9.68 ± 13.78	1.53 ± 0.27	64.5 ± 18.29	0.69 ± 0.36
40749395	11.97	2.47 ± 0.13	6254 ± 188	SG	3.0258 ± 0.0012	2723.2045 ± 0.005	0.0531 ± 0.028	14.31 ± 0.75	5.78 ± 0.54	86.2 ± 2.7	0.39 ± 0.29
452072538	11.92	2.09 ± 0.10	6220 ± 135	SG	6.3226 ± 0.0065	2311.4728 ± 0.0082	0.0866 ± 0.0333	19.8 ± 7.6	5.8 ± 2.5	82.6 ± 5.3	0.75 ± 0.2
453142142	11.63	2.42 ± 0.14	6221 ± 120	SG	1.70454 ± 0.00057	2203.0845 ± 0.0057	0.0349 ± 0.0034	9.18 ± 0.9	5.31 ± 0.81	84.8 ± 3.7	0.48 ± 0.31
466314014	11.57	2.14 ± 0.19	6008 ± 133	SG	2.89972 ± 0.0036	2797.432 ± 0.002	0.077 ± 0.0025	17.95 ± 0.58	5.81 ± 0.31	86.8 ± 2.2	0.33 ± 0.23
466890210	11.71	2.59 ± 0.14	6018 ± 146	SG	5.1871 ± 0.0023	2799.5792 ± 0.0063	0.0577 ± 0.0027	16.31 ± 0.74	5.57 ± 0.41	85.8 ± 2.9	0.39 ± 0.28
685340263	10.31	1.80 ± 0.08	6033 ± 135	SG	5.0607 ± 0.0028	2119.724 ± 0.0114	0.0655 ± 0.0014	12.9 ± 0.28	6.26 ± 0.18	87.7 ± 1.6	0.25 ± 0.22
13202532	10.87	3.48	5259 ± 76	ERG	5.5403 ± 0.0013	2177.2393 ± 0.0033	0.0506 ± 0.0012	19.17 ± 0.47	4.74 ± 0.65	83.7 ± 4.0	0.52 ± 0.16
86894845	11.28	2.64	4973 ± 122	ERG	4.24021 ± 0.0021	2475.194 ± 0.0118	0.0531 ± 0.0016	15.26 ± 0.47	8.51 ± 0.63	87.4 ± 1.8	0.38 ± 0.26
21885662	10.95	2.26	5247 ± 122	ERG	1.12942 ± 0.0082	2362.9833 ± 0.0103	0.0439 ± 0.0069	10.8 ± 6.6	5.37 ± 0.94	85.8 ± 4.5	0.39 ± 0.27
251006970	10.97	4.62	4558 ± 122	ERG	1.1399 ± 0.0075	2770.4044 ± 0.0086	0.0439 ± 0.0053	22.1 ± 16.0	1.82 ± 0.6	59.25 ± 24.43	0.84 ± 0.57
268320188	10.80	3.46	4917 ± 122	ERG	10.0248 ± 0.0034	2394.6478 ± 0.0098	0.0306 ± 0.0016	11.56 ± 1.03	2.01 ± 0.62	64.19 ± 20.57	0.83 ± 0.49
291493871	10.72	4.85	4826 ± 122	ERG	1.15626 ± 0.0076	2201.8922 ± 0.0095	0.0244 ± 0.0003	12.9 ± 1.1	1.75 ± 0.24	74.39 ± 11.03	0.48 ± 0.33
30333591	11.43	4.44	5032 ± 122	ERG	3.55074 ± 0.0065	2282.9612 ± 0.0044	0.0408 ± 0.0033	19.8 ± 1.6	5.67 ± 0.62	85.5 ± 3.3	0.45 ± 0.31
397187844	11.52	3.26	4968 ± 122	ERG	8.41795 ± 0.0038	2285.649 ± 0.0108	0.0383 ± 0.0077	13.6 ± 13.4	3.9 ± 3.0	77.15 ± 10.59	0.86 ± 0.51
								13.6 ± 3.0	0.0084		0.86 ± 0.59

* SG: sub-giant sub-population; ERG: early red giant sub-population

Table A2: Stellar and planetary properties for the TOI planet candidates we independently detect with our planet search pipeline and their host stars

TIC	TOI	T (mag)	R_* (R_{\odot})/TIC)	T_{eff} (K_{\odot})/TIC)	Sub-Population*	P (days)	$T_C - 247000$	R_p/R_*	R_p/R_{\oplus}	a/R_*	i (degrees)	b
13737885	3382	11.55	2.16 ± 0.11	6329 ± 119	SG	4.4574 ± 0.0013	2236.0817 ± 0.0025	0.0637 ± 0.0015	15.0 ± 0.35	5.72 ± 0.88	85.3 ± 3.2	0.47 ± 0.2
14156936	5340	11.71	1.69 ± 0.08	6287 ± 107	SG	4.9392 ± 0.0017	2450.7911 ± 0.0015	0.0747 ± 0.0014	13.78 ± 0.36	8.0 ± 0.28	88.1 ± 1.3	0.26 ± 0.23
2112157	5365	11.04	2.76 ± 0.17	6080 ± 137	SG	4.00774 ± 0.0063	2449.2678 ± 0.0005	0.0328 ± 0.0022	9.86 ± 0.67	4.33 ± 0.53	83.6 ± 4.5	0.49 ± 0.28
28961316	3682	11.32	1.91 ± 0.10	5501 ± 125	SG	3.346539 ± 9.8e-05	2448.3827 ± 0.0012	0.0675 ± 0.0016	14.07 ± 0.33	6.27 ± 0.32	87.0 ± 2.1	0.33 ± 0.22
32439194	6777	11.97	1.90 ± 0.11	6288 ± 152	SG	3.36111 ± 0.0058	2037.6528 ± 0.0021	0.08833 ± 0.0026	17.28 ± 0.54	5.47 ± 0.44	85.3 ± 3.0	0.41 ± 0.24
33227166	4999	10.82	1.99 ± 0.10	5698 ± 128	SG	5.5832 ± 0.0051	2366.0549 ± 0.0146	0.04833 ± 0.0033	10.49 ± 0.85	7.2 ± 1.0	86.3 ± 2.6	0.46 ± 0.31
88886876	5432	11.44	1.48 ± 0.08	5612 ± 124	SG	5.48889 ± 0.0038	2475.4876 ± 0.002	0.06732 ± 0.0096	18.62 ± 0.26	6.08 ± 0.23	87.3 ± 1.8	0.28 ± 0.19
5832253	5328	11.23	2.54 ± 0.12	6120 ± 101	SG	3.346539 ± 9.8e-05	2448.3827 ± 0.0019	0.06732 ± 0.0013	10.28	6.47	87.0 ± 2.2	0.33 ± 0.22
81077799	3492	8.45	2.59 ± 0.11	6332 ± 134	SG	9.2226 ± 0.0035	2286.8431 ± 0.0009	0.05056 ± 0.0019	14.3 ± 0.36	14.05 ± 0.53	88.8 ± 0.82	0.29 ± 0.24
85266608	5385	10.86	2.08 ± 0.10	6238 ± 124	SG	5.1676 ± 0.0012	2613.4016 ± 0.0033	0.06535 ± 0.0037	14.8 ± 0.84	5.84 ± 0.96	84.3 ± 3.6	0.38 ± 0.17
97714451	4734	11.90	1.76 ± 0.11	5854 ± 149	SG	6.235064 ± 6.4e-05	2205.1508 ± 0.0029	0.0557 ± 0.0013	10.55 ± 0.24	12.83 ± 0.41	7.41 ± 0.42	0.34 ± 0.24
131348451	3414	11.97	1.81 ± 0.09	6259 ± 139	SG	9.7358 ± 0.0025	2235.5667 ± 0.0054	0.0548 ± 0.0037	10.79 ± 0.73	10.51 ± 1.5	8.05 ± 0.95	0.34 ± 0.23
141363913	601	9.92	3.10 ± 0.26	6221 ± 133	SG	3.34565 ± 0.0041	2236.9457 ± 0.0014	0.0774 ± 0.0014	14.74 ± 0.27	6.8 ± 0.64	87.6 ± 1.7	0.29 ± 0.22
1433257668	5679	11.20	1.61 ± 0.09	6152 ± 131	SG	8.4336 ± 0.0013	2479.1328 ± 0.0057	0.0475 ± 0.003	12.72 ± 0.79	6.71 ± 1.34	86.0 ± 2.8	0.47 ± 0.24
193754373	4487	11.49	1.69 ± 0.08	6006 ± 156	SG	1.6622 ± 0.0016	2037.108 ± 0.0012	0.10353 ± 0.0023	18.5 ± 0.41	3.77 ± 0.16	85.5 ± 3.6	0.47 ± 0.31
202941251	5891	11.39	2.40 ± 0.12	6283 ± 153	SG	3.954057 ± 7.8e-05	2422.6466 ± 0.0012	0.081 ± 0.0026	14.97 ± 0.46	7.3 ± 0.49	87.8 ± 1.5	0.32 ± 0.25
215018906	5217	11.00	2.45 ± 0.14	5874 ± 168	SG	3.47488 ± 0.0014	2258.5743 ± 0.0005	0.0354 ± 0.0036	11.96 ± 0.22	10.3 ± 1.8	87.2 ± 2.0	0.32 ± 0.22
221785300	3489	11.72	1.23 ± 0.07	5266 ± 128	SG	9.03948 ± 8.4e-05	2422.4978 ± 0.0019	0.0703 ± 0.0037	18.41 ± 0.97	5.68 ± 1.18	83.5 ± 3.8	0.51 ± 0.34
232982938	1828	11.13	1.56 ± 0.08	5809 ± 127	SG	4.17847 ± 2.5e-05	2422.4978 ± 0.0018	0.0354 ± 0.0026	10.3 ± 1.8	8.7 ± 2.4	80.5 ± 0.32	0.51 ± 0.32
238197638	903	11.79	2.21 ± 0.10	6147 ± 111	SG	4.37128 ± 4.9e-05	2395.2025 ± 0.0002	0.0606 ± 0.0022	16.2 ± 0.76	6.91 ± 1.62	86.0 ± 2.8	0.48 ± 0.23
238920875	2329	11.79	1.33 ± 0.08	5218 ± 133	SG	6.5354667 ± 4.2e-05	2064.4841 ± 0.0011	0.0783 ± 0.0014	11.35 ± 0.32	8.7 ± 0.27	88.5 ± 1.0	0.29 ± 0.19
258510872	1885	11.97	1.76 ± 0.08	6232 ± 123	SG	6.544057 ± 6.4e-05	2612.6614 ± 0.001	0.0742 ± 0.0012	14.23 ± 0.24	7.3 ± 0.85	87.2 ± 1.9	0.36 ± 0.21
282221346	5042	11.04	2.32 ± 0.11	5784 ± 129	SG	5.63204 ± 0.0006	2338.3784 ± 0.0031	0.0458 ± 0.0019	10.51 ± 0.36	6.16 ± 0.12	88.9 ± 0.7	0.26 ± 0.21
291517604	5148	10.01	1.91 ± 0.10	5447 ± 127	SG	7.27660 ± 5.8e-05	2039.8831 ± 0.0014	0.0598 ± 0.0021	13.69 ± 0.51	9.1 ± 1.9	86.4 ± 2.4	0.64 ± 0.12
294768072	5062	11.81	2.08 ± 0.11	5693 ± 115	SG	6.5354667 ± 4.2e-05	2064.4841 ± 0.0011	0.0783 ± 0.0014	11.35 ± 0.32	6.9 ± 0.84	86.0 ± 2.8	0.48 ± 0.23
306248357	6538	11.93	1.83 ± 0.09	6219 ± 130	SG	5.7218 ± 0.0047	2310.9598 ± 0.0071	0.05151 ± 0.0009	8.78 ± 0.15	14.79 ± 0.5	8.89 ± 0.8	0.22 ± 0.16
306357884	3322	11.56	2.53 ± 0.21	6307 ± 130	SG	1.0571 ± 0.0016	2363.3405 ± 0.0036	0.0458 ± 0.0014	13.69 ± 0.51	9.1 ± 1.9	86.6 ± 2.4	0.64 ± 0.12
315096343	2978	11.67	1.88 ± 0.10	5734 ± 126	SG	5.0642 ± 0.0041	2362.8529 ± 0.0012	0.0666 ± 0.0022	16.2 ± 0.6	6.91 ± 1.62	86.0 ± 2.8	0.48 ± 0.23
334495570	777	9.37	1.60 ± 0.08	6187 ± 137	SG	6.2292 ± 0.0053	2367.6937 ± 0.011	0.0429 ± 0.0078	13.57 ± 0.32	8.7 ± 0.27	88.5 ± 1.0	0.22 ± 0.16
371864043	3041	11.26	1.84 ± 0.09	6268 ± 121	SG	3.97218 ± 0.0047	2310.9598 ± 0.0071	0.0524 ± 0.0012	10.44 ± 0.74	7.3 ± 0.49	87.2 ± 1.9	0.36 ± 0.21
379824738	5810	10.29	1.87 ± 0.09	6142 ± 132	SG	5.68339 ± 0.0042	2797.7146 ± 0.0012	0.07319 ± 0.0099	12.12 ± 1.58	5.4 ± 1.1	86.2 ± 2.4	0.41 ± 0.25
397763985	5765	11.54	1.57 ± 0.08	5798 ± 214	SG	3.8782 ± 0.0001	2722.4911 ± 0.0031	0.0696 ± 0.0002	11.92 ± 1.06	6.4 ± 1.3	88.5 ± 1.9	0.19 ± 0.16
404467699	857	10.27	1.63 ± 0.08	6143 ± 131	SG	3.90849 ± 0.0023	2118.2899 ± 0.0068	0.0872 ± 0.0018	15.52 ± 0.32	6.4 ± 1.3	84.4 ± 1.1	0.67 ± 0.37

Continued on next page

Table A2 – continued from previous page

TIC	TOI	T (mag)	R_* (R _⊕ ·TIC)	T_{eff} (K·TIC)	Sub-Population*	P (days)	$T_C - 2457000$	R_p / R_*	R_p / R_{\oplus}	a / R_*	i (degrees)	b
409594381	4214	11.01	1.59 ± 0.08	5.806 ± 174	SG	3.49122 ± 0.00016	2203.546 ± 0.0011	0.0652 ± 0.002	11.45 ± 0.35	8.47 ± 0.46	87.7 ± 1.6	0.34 ± 0.26
420268415	4436	11.89	2.00 ± 0.09	6.250 ± 136	SG	1.7590562 ± 2.5e-06	2392.92077 ± 0.00038	0.0980 ± 0.009	21.38 ± 0.17	4.137 ± 0.15	86.8 ± 2.1	0.23 ± 0.13
436102447	2359	11.03	2.70 ± 0.14	6.130 ± 120	SG	5.18706 ± 0.00094	2176.3256 ± 0.0025	0.0639 ± 0.0015	18.8 ± 0.49	5.32 ± 0.36	85.8 ± 2.9	0.39 ± 0.22
436637677	4705	11.46	1.77 ± 0.09	6.266 ± 148	SG	11.91384 ± 0.00014	2185.5327 ± 0.0031	0.0714 ± 0.002	13.79 ± 0.37	16.62 ± 2.21	88.89 ± 0.77	0.32 ± 0.26
440872576	3160	11.93	1.62 ± 0.12	6.200 ± 125	SG	3.97095 ± 0.0004	2335.9688 ± 0.0015	0.0874 ± 0.0035	15.44 ± 0.94	10.5 ± 1.2	87.4 ± 1.8	0.47 ± 0.26
448435566	4951	11.84	1.92 ± 0.09	5.823 ± 125	SG	4.1027 ± 0.0013	2337.3539 ± 0.0049	0.0599 ± 0.0031	12.55 ± 0.65	5.51 ± 0.88	84.4 ± 4.1	0.54 ± 0.25
446370039	3499	11.52	3.12 ± 0.18	5.695 ± 132	ERG	4.59870 ± 0.0006	2284.9679 ± 0.0038	0.0559 ± 0.0014	19.04 ± 0.48	4.07 ± 0.44	83.7 ± 4.7	0.49 ± 0.21

* SG: sub-giant sub population ; ERG: early red giant sub-population

Table A3: Stellar and planetary properties for the known planets we independently detect with our planet search pipeline and their host stars

TIC	Planet	T (mag)	R_* (R _⊕ ·TIC)	T_{eff} (K·TIC)	Sub-Population*	P (days)	$T_C - 2457000$	R_p / R_*	R_p / R_{\oplus}	a / R_*	i (degrees)	b	Reference
17746821	HAT-P-50b	11.32	1.73 ± 0.11	6.322 ± 143	SG	3.121989 ± 1.1e-05	2229.96168 ± 0.00088	0.0788 ± 0.0023	14.86 ± 0.44	5.76 ± 0.82	84.0 ± 2.8	0.606 ± 0.097	Hartman et al. (2015)
20096620	HAT-P-13b	9.96	1.83 ± 0.09	5.720 ± 119	SG	2.916382 ± 8.3e-05	2582.97935 ± 0.0004	0.0859 ± 0.0015	17.11 ± 0.37	5.6 ± 0.33	82.66 ± 0.94	0.716 ± 0.034	Bakos et al. (2009)
44725334	TOL-954b	9.78	1.93 ± 0.10	5.756 ± 127	SG	3.6825 ± 0.0003	2145.2174 ± 0.0012	0.04616 ± 0.0019	9.73 ± 0.23	5.91 ± 0.23	87.2 ± 1.9	0.29 ± 0.22	Shao et al. (2021)
51234631	XO-4-b	10.17	1.62 ± 0.09	6.304 ± 140	SG	4.12322 ± 0.00014	2584.51491 ± 0.0041	0.08787 ± 0.0068	15.55 ± 0.12	7.7 ± 0.27	88.37 ± 0.98	0.19 ± 0.13	McCullough et al. (2008)
68007716	TOI-2587 A b	10.97	1.72 ± 0.10	5.776 ± 137	SG	5.4574 ± 0.0012	2233.83688 ± 0.0022	0.0615 ± 0.0018	11.52 ± 0.34	10.53 ± 0.49	88.4 ± 1.1	0.3 ± 0.24	Yee et al. (2023)
69356857	TOI-5232b	11.78	1.74 ± 0.08	6.212 ± 128	SG	4.096625 ± 1.9e-05	2390.9111 ± 0.0014	0.0709 ± 0.0015	13.46 ± 0.32	6.67 ± 0.28	87.5 ± 1.7	0.3 ± 0.21	Schulte et al. (2024)
70524163	TOI-2421b	10.69	1.79 ± 0.10	5.618 ± 132	SG	4.3478 ± 0.00058	2117.8801 ± 0.0019	0.0556 ± 0.0003	10.86 ± 0.58	6.18 ± 0.8	85.3 ± 3.2	0.51 ± 0.21	Yee et al. (2022)
71756657	WASP-159b	11.88	2.04 ± 0.09	5.977 ± 130	SG	3.84055 ± 0.00019	2146.64643 ± 0.0015	0.0736 ± 0.0019	16.36 ± 0.41	4.93 ± 0.4	85.1 ± 3.3	0.42 ± 0.17	Heller et al. (2019)
88992642	TOI-2145b	8.56	2.78 ± 0.13	6.202 ± 130	SG	10.26132 ± 3.3e-05	2392.9417 ± 0.0009	0.04367 ± 0.0007	13.25 ± 0.21	8.75 ± 1.08	85.99 ± 1.4	0.612 ± 0.076	Rodriguez et al. (2023)
9235220	WASP-94 A b	9.64	1.71 ± 0.07	6.073 ± 106	SG	3.9501 ± 0.00012	2039.33526 ± 0.0036	0.10633 ± 0.0023	15.84 ± 0.14	7.349 ± 0.27	89.11 ± 0.62	0.115 ± 0.13	Ne-Van-Malle et al. (2014)
97755908	KELT2-A b	8.22	1.88 ± 0.09	6.327 ± 132	SG	4.113764 ± 2.0e-05	2475.42662 ± 0.0002	0.06933 ± 0.0037	14.195 ± 0.077	6.607 ± 0.083	88.48 ± 1.0	0.17 ± 0.11	Beatty et al. (2012)
99869022	TOI-1199b	10.42	1.54 ± 0.08	5.618 ± 122	SG	3.671434 ± 1.7e-05	2420.53888 ± 0.00062	0.06566 ± 0.0018	10.98 ± 0.3	7.74 ± 1.07	83.86 ± 1.23	0.827 ± 0.034	Serrano Bell et al. (2024)
100566492	WASP-88b	11.12	1.99 ± 0.09	6.282 ± 106	SG	4.9535 ± 0.0009	2040.9075 ± 0.0015	0.08633 ± 0.0012	18.74 ± 0.26	6.74 ± 0.15	88.4 ± 1.1	0.19 ± 0.18	Deleze et al. (2014)
122612091	WASP-72b	10.46	2.66 ± 0.13	5.773 ± 111	SG	2.216706 ± 4.9e-05	2117.14139 ± 0.0067	0.06665 ± 0.0012	19.3 ± 0.36	3.597 ± 0.31	78.97 ± 2.2	0.694 ± 0.045	Gillon et al. (2013)
138294130	HAT-P-4-b	10.65	1.60 ± 0.07	5.981 ± 117	SG	3.056495 ± 0.00019	2671.14452 ± 0.0061	0.0849 ± 0.0019	14.8 ± 0.33	5.68 ± 0.21	87.0 ± 2.2	0.29 ± 0.18	Kovács et al. (2007)
139528693	WASP-78b	11.83	2.06 ± 0.10	6.291 ± 130	SG	2.175262 ± 5.1e-05	2145.13632 ± 0.0074	0.0829 ± 0.0082	18.65 ± 0.19	3.819 ± 0.058	87.4 ± 1.8	0.17 ± 0.15	Smalley et al. (2012)
157230659	NGTS-12b	11.66	1.53 ± 0.07	5.869 ± 124	SG	7.53206 ± 0.00056	2288.46597 ± 0.0018	0.0682 ± 0.0011	11.37 ± 0.18	10.59 ± 0.26	88.83 ± 0.8	0.22 ± 0.18	Bryan et al. (2020)
159742538	TExS-4-b	11.11	2.01 ± 0.10	6.184 ± 138	SG	3.553394 ± 7.3e-06	2391.21043 ± 0.0053	0.09666 ± 0.0015	21.16 ± 0.33	5.97 ± 0.43	82.63 ± 1.03	0.765 ± 0.031	Mandushev et al. (2007)
166236920	WASP-99b	8.93	1.71 ± 0.08	6.079 ± 132	SG	5.752398 ± 7.7e-05	2089.7512 ± 0.0004	0.06914 ± 0.0034	12.89 ± 0.63	8.785 ± 0.062	89.26 ± 0.51	0.113 ± 0.09	Heller et al. (2014)
176207877	WASP-136b	9.48	2.39 ± 0.12	6.067 ± 120	SG	5.215357 ± 1.1e-05	2092.52423 ± 0.0046	0.06915 ± 0.0054	18.03 ± 0.14	7.6 ± 0.13	88.5 ± 1.0	0.19 ± 0.16	Lam et al. (2017)
211438925	WASP-20b	10.25	1.50	5.776	SG	4.89665 ± 0.0024	2091.51188 ± 0.0063	0.0983 ± 0.0025	16.13 ± 0.41	10.49 ± 0.09	86.82 ± 1.14	0.581 ± 0.081	Anderson et al. (2015)
219015370	TOI-294b	10.95	1.58 ± 0.08	5.714 ± 126	SG	3.91527 ± 2e-05	2393.00789 ± 0.0009	0.0606 ± 0.0018	10.45 ± 0.31	6.45 ± 0.68	82.48 ± 1.12	0.845 ± 0.027	Polanski et al. (2024)
219854185	TOI-1296b	10.80	1.75 ± 0.09	5.494 ± 126	SG	3.944391 ± 5.6e-06	2392.24607 ± 0.0048	0.07677 ± 0.0093	14.69 ± 0.18	6.53 ± 0.12	88.1 ± 1.3	0.21 ± 0.14	Montou et al. (2021)
229118866	TOI-1181b	10.08	1.93 ± 0.09	6.122 ± 125	SG	2.103192 ± 1.2e-06	2391.07951 ± 0.0016	0.07785 ± 0.0053	16.36 ± 0.11	4.14 ± 0.10	86.3 ± 1.9	0.27 ± 0.09	Kabath et al. (2022)
231670397	WASP-73b	9.86	2.22 ± 0.10	6.124 ± 134	SG	4.08758 ± 0.0032	2038.86395 ± 0.0093	0.05755 ± 0.0101	13.93 ± 0.24	5.56 ± 0.37	86.0 ± 2.6	0.39 ± 0.16	Delrez et al. (2014)
237104103	TOI-298b	10.96	1.49 ± 0.07	5.731 ± 125	SG	4.537122 ± 9.3e-06	2392.37499 ± 0.0057	0.06271 ± 0.0063	10.17 ± 0.13	8.89 ± 0.27	88.3 ± 1.1	0.27 ± 0.17	Montou et al. (2021)

Continued on next page

* SG: sub-giant sub population ; ERG: early red giant sub-population

Table A3 – continued from previous page

TIC	Planet	T (mag)	R_* (R _⊕ ·TIC)	T_{eff} (K·TIC)	Sub-Population*	P (days)	$T_C - 2457000$	R_p/R_*	$R_p(R_{\oplus})$	a/R_*	i (degrees)	b	Reference
257066897	TIC 257066897 b	11.26	1.89 ± 0.09	6019 ± 123	SG	3.6600368 ^{+8.1e-06} _{-8.1e-06}	2393.42489 ^{+0.00048} _{-0.00047}	0.0852 ^{+0.0024} _{-0.0027}	1.754 ^{+0.49} _{-0.55}	5.66 ^{+0.51} _{-0.42}	84.9 ^{+2.4} _{-1.7}	0.5 ^{+0.12} _{-0.22}	Montalto et al. (2022)
23820431	TOI-2567 b	11.75	1.72 ± 0.09	5609 ± 130	SG	5.93891 ^{+2.2e-05} _{-2.2e-05}	2396.7393 ^{+0.00012} _{-0.00012}	0.05926 ^{+0.00081} _{-0.00076}	1.1 ^{+0.15} _{-0.14}	8.78 ^{+0.44} _{-0.44}	88.75 ^{+0.87} _{-1.28}	0.19 ^{+0.18} _{-0.13}	Yee et al. (2022)
27189367	TOI-150 b	10.90	1.68 ± 0.07	5983 ± 109	SG	5.857429 ^{+1.3e-05} _{-1.3e-05}	2040.8851 ^{+0.00042} _{-0.00042}	0.07889 ^{+0.00075} _{-0.00075}	1.4 ^{+0.12} _{-0.12}	7.63 ^{+0.28} _{-0.28}	86.86 ^{+0.78} _{-0.57}	0.419 ^{+0.061} _{-0.092}	Kossakowski et al. (2019)
281731203	K2-261 b	9.96	1.73 ± 0.09	5466 ± 126	SG	11.63372 ^{+7.3e-05} _{-7.3e-05}	2267.9521 ^{+0.00105} _{-0.00105}	0.052833 ^{+0.00119} _{-0.00095}	10.0 ^{+0.23} _{-0.18}	17.34 ^{+1.61} _{-1.52}	89.13 ^{+0.85} _{-0.85}	0.26 ^{+0.21} _{-0.18}	Johnson et al. (2018)
284475976	WASP-48 b	11.15	1.77 ± 0.09	6148 ± 141	SG	2.143686 ^{+2.5e-06} _{-2.4e-06}	2392.44558 ^{+0.00033} _{-0.00035}	0.09444 ^{+0.0015} _{-0.0023}	18.24 ^{+0.29} _{-0.45}	4.84 ^{+0.32} _{-0.22}	82.9 ^{+1.6} _{-1.0}	0.601 ^{+0.054} _{-0.103}	Enoch et al. (2011)
286923464	HD 118023 b	7.46	2.05 ± 0.11	5837 ± 140	SG	6.13515 ^{+0.00025} _{-0.00025}	2645.1791 ^{+0.00046} _{-0.00046}	0.05667 ^{+0.00041} _{-0.00036}	12.679 ^{+0.93} _{-0.82}	8.65 ^{+0.11} _{-0.3}	88.91 ^{+0.76} _{-1.04}	0.16 ^{+0.15} _{-0.11}	da Silva et al. (2006)
322307342	HATS-68 b	11.78	2.00 ± 0.11	5705 ± 125	SG	3.58615 ^{+0.00015} _{-0.00015}	2063.657 ^{+0.0012} _{-0.0012}	0.0757 ^{+0.0015} _{-0.0027}	16.54 ^{+0.32} _{-0.59}	5.94 ^{+1.17} _{-0.42}	82.39 ^{+2.5} _{-0.95}	0.786 ^{+0.036} _{-0.154}	Hartman et al. (2019)
339672028	TOI-481 b	9.39	1.73 ± 0.09	5803 ± 134	SG	10.33 ^{+1.2e-05} _{-1.2e-05}	2038.53073 ^{+0.00052} _{-0.00052}	0.06309 ^{+0.00048} _{-0.00037}	11.893 ^{+0.091} _{-0.07}	14.61 ^{+0.2} _{-0.52}	89.31 ^{+0.48} _{-0.61}	0.18 ^{+0.14} _{-0.12}	Brahm et al. (2020)
342642028	TOI-2158 b	10.17	1.50 ± 0.08	5389 ± 123	SG	8.600729 ^{+5.8e-05} _{-6.3e-05}	2397.3563 ^{+0.00018} _{-0.00015}	0.06554 ^{+0.0003} _{-0.00027}	10.67 ^{+0.49} _{-0.46}	17.67 ^{+2.4} _{-2.3}	88.3 ^{+1.1} _{-1.2}	0.52 ^{+0.21} _{-0.32}	Kundurup et al. (2022)
375942197	WASP-176 b	11.54	1.86 ± 0.10	6152 ± 134	SG	3.89946 ^{+0.00046} _{-0.00046}	2797.7001 ^{+0.00105} _{-0.00105}	0.0786 ^{+0.0014} _{-0.0015}	15.97 ^{+0.31} _{-0.31}	6.0 ^{+0.23} _{-0.23}	87.3 ^{+1.8} _{-2.4}	0.28 ^{+0.19} _{-0.11}	Cooke et al. (2020)
386259537	WASP-169 b	11.33	2.21 ± 0.11	6158 ± 130	SG	5.6102 ^{+0.00013} _{-0.00013}	2234.3457 ^{+0.0024} _{-0.0024}	0.0745 ^{+0.002} _{-0.0018}	17.98 ^{+0.44} _{-0.44}	6.92 ^{+0.76} _{-0.74}	87.3 ^{+1.8} _{-2.4}	0.32 ^{+0.22} _{-0.22}	Nielsen et al. (2019)
39314358	WASP-63 b	10.44	1.79 ± 0.10	5715 ± 129	SG	4.378082 ^{+7.6e-05} _{-7.6e-05}	2174.5682 ^{+0.00057} _{-0.00056}	0.0798 ^{+0.00095} _{-0.00095}	15.6 ^{+0.19} _{-0.14}	5.56 ^{+0.14} _{-0.29}	88.0 ^{+1.3} _{-1.5}	0.22 ^{+0.15} _{-0.15}	Heller et al. (2012)
394722182	TOI-2236 b	10.87	1.62 ± 0.07	6209 ± 127	SG	3.5315806 ^{+7.7e-06} _{-7.6e-06}	2039.71045 ^{+0.00053} _{-0.00054}	0.08614 ^{+0.00114} _{-0.00098}	15.26 ^{+0.2} _{-0.17}	0.84 ^{+0.34} _{-0.29}	83.5 ^{+0.56} _{-0.5}	0.774 ^{+0.025} _{-0.032}	Yee et al. (2022)
422655579	WASP-71 b	10.16	2.14 ± 0.10	6180 ± 113	SG	2.90354 ^{+9.3e-05} _{-9.4e-05}	2449.75839 ^{+0.0008} _{-0.0008}	0.06062 ^{+0.00103} _{-0.00086}	15.43 ^{+0.24} _{-0.2}	4.49 ^{+0.19} _{-0.33}	86.0 ^{+2.7} _{-2.7}	0.39 ^{+0.17} _{-0.17}	Smith et al. (2013)
454248975	TOI-3023 b	11.48	1.69 ± 0.09	5512 ± 127	SG	3.90158 ^{+0.0016} _{-0.0016}	2313.0843 ^{+0.0011} _{-0.0011}	0.09 ^{+0.0017} _{-0.0013}	16.56 ^{+0.3} _{-0.24}	0.36 ^{+0.15} _{-0.32}	88.1 ^{+1.3} _{-1.8}	0.21 ^{+0.18} _{-0.14}	Yee et al. (2023)
459730973	WASP-90 b	11.07	1.84 ± 0.11	6228 ± 129	SG	3.91669 ^{+0.00096} _{-0.00096}	2799.3644 ^{+0.00109} _{-0.00108}	0.0843 ^{+0.0043} _{-0.0036}	16.91 ^{+0.87} _{-1.13}	6.3 ^{+1.56} _{-0.79}	82.8 ^{+2.7} _{-1.7}	0.791 ^{+0.067} _{-0.169}	West et al. (2016)
176956883	TOI-2184 b	11.41	3.15 ± 0.17	5721 ± 123	ERG	6.9066868 ^{+8.0e-05} _{-8.2e-05}	2036.6195 ^{+0.00224} _{-0.00224}	0.04194 ^{+0.00124} _{-0.00092}	14.41 ^{+0.43} _{-0.32}	7.26 ^{+0.74} _{-1.18}	86.4 ^{+2.4} _{-2.7}	0.45 ^{+0.21} _{-0.29}	Saunders et al. (2022)
230001847	TOI-2337 b	11.23	3.23	4784 ± 122	ERG	2.99422 ^{+3.7e-05} _{-3.8e-05}	2392.6794 ^{+0.0033} _{-0.0034}	0.0382 ^{+0.0018} _{-0.0022}	12.44 ^{+0.65} _{-0.77}	2.15 ^{+0.47} _{-0.25}	67.7 ^{+7.6} _{-4.9}	0.813 ^{+0.056} _{-0.152}	Grundblatt et al. (2022)
394918211	TOI-4377 b	10.79	3.41	4913 ± 122	ERG	4.37702 ^{+0.00056} _{-0.00053}	2337.6436 ^{+0.00336} _{-0.00338}	0.03894 ^{+0.0012} _{-0.00099}	14.5 ^{+0.45} _{-0.37}	4.0 ^{+0.23} _{-0.23}	85.0 ^{+3.5} _{-4.6}	0.35 ^{+0.23} _{-0.24}	Pereira et al. (2024)

*: SG: sub-giant sub-population ; ERG: early red giant sub-population

Table A4: Stellar and planetary properties for the small planets ($R_p \leq 8 R_{\oplus}$) we detect with our planet search pipeline, but do not include in our occurrence rate measurements, and their host stars

TIC	TOI	Planet	T (mag)	R_* (R _⊕ ; TIC)	T_{eff} (K; TIC)	Sub-Population*	P (days)	$T_C - 2457000$	R_p/R_*	$R_p(R_{\oplus})$	a/R_*	i (degrees)	b
3317218			9.18	1.83 ± 0.09	5646 ± 204	SG	2.77493 ^{+0.00075} _{-0.00066}	2475.266 ^{+0.00086} _{-0.0109}	0.01298 ^{+0.00134} _{-0.00097}	2.61 ^{+0.27} _{-0.2}	4.08 ^{+0.68} _{-1.15}	83.2 ^{+4.8} _{-9.0}	0.49 ^{+0.31} _{-0.33}
16976334			10.69	1.61 ± 0.08	5560 ± 123	SG	5.70446 ^{+0.00021} _{-0.00021}	2090.748 ^{+0.00045} _{-0.0055}	0.0324 ^{+0.0027} _{-0.0022}	5.69 ^{+0.47} _{-0.38}	9.4 ^{+1.6} _{-3.0}	86.9 ^{+2.2} _{-4.3}	0.51 ^{+0.31} _{-0.34}
198186769	1291		10.87	1.81 ± 0.08	6229 ± 124	SG	7.161999 ^{+0.00111} _{-0.3e-05}	2397.8154 ^{+0.00333} _{-0.00339}	0.03048 ^{+0.00177} _{-0.00177}	6.02 ^{+0.23} _{-0.15}	6.37 ^{+0.48} _{-1.17}	86.5 ^{+2.5} _{-3.9}	0.39 ^{+0.28} _{-0.27}
245893485			11.26	1.70 ± 0.09	5559 ± 131	SG	1.38348 ^{+0.00083} _{-0.00083}	2363.2384 ^{+0.00082} _{-0.00082}	0.0408 ^{+0.0066} _{-0.0036}	7.58 ^{+1.23} _{-0.67}	3.5 ^{+0.64} _{-0.67}	81.6 ^{+5.9} _{-13.9}	0.52 ^{+0.34} _{-0.35}
298189384			11.45	1.54 ± 0.08	5876 ± 138	SG	9.06049 ^{+0.00639} _{-0.00632}	2425.744 ^{+0.015} _{-0.015}	0.0388 ^{+0.0049} _{-0.0032}	6.5 ^{+0.83} _{-0.54}	8.3 ^{+1.8} _{-3.0}	86.4 ^{+2.6} _{-5.7}	0.53 ^{+0.32} _{-0.36}
350020859	HD 89345 b		8.75	1.79 ± 0.09	5609 ± 129	SG	11.81458 ^{+0.00081} _{-0.00081}	2532.3756 ^{+0.00116} _{-0.00116}	0.0368 ^{+0.00115} _{-0.00079}	7.17 ^{+0.22} _{-0.15}	15.6 ^{+1.2} _{-2.5}	88.57 ^{+0.99} _{-1.34}	0.39 ^{+0.24} _{-0.26}
350033870	5177		8.85	1.68 ± 0.08	6183 ± 128	SG	2.20703 ^{+0.00101} _{-0.00101}	2526.307 ^{+0.00205} _{-0.00205}	0.01375 ^{+0.00099} _{-0.00099}	2.52 ^{+0.38} _{-0.17}	3.01 ^{+0.5} _{-1.08}	79.6 ^{+7.4} _{-16.8}	0.55 ^{+0.33} _{-0.37}
366804698	5646		10.88	1.93 ± 0.11	5999 ± 134	SG	2.4278 ^{+0.00113} _{-0.00101}	2448.236 ^{+0.018} _{-0.018}	0.0354 ^{+0.0028} _{-0.0019}	7.02 ^{+0.58} _{-0.39}	4.74 ^{+0.62} _{-1.31}	84.3 ^{+4.0} _{-7.5}	0.47 ^{+0.31} _{-0.32}
381360757	5069		9.64	1.87 ± 0.09	6332 ± 126	SG	8.8608 ^{+0.0027} _{-0.0029}	2448.236 ^{+0.018} _{-0.018}	0.0188 ^{+0.0025} _{-0.0025}	3.84 ^{+0.51} _{-0.31}	7.8 ^{+1.5} _{-2.9}	86.2 ^{+2.8} _{-6.0}	0.53 ^{+0.32} _{-0.36}
40093769			11.17	1.69	5843	SG	3.6023 ^{+0.00116} _{-0.00116}	2745.8379 ^{+0.00063} _{-0.00063}	0.0425 ^{+0.0043} _{-0.0031}	7.84 ^{+0.57} _{-0.57}	8.5 ^{+1.6} _{-2.9}	86.4 ^{+2.6} _{-5.3}	0.53 ^{+0.31} _{-0.35}
408618999	TOI-1736 b		8.33	1.41 ± 0.07	5656 ± 123	SG	7.073 ^{+0.003} _{-0.0028}	2726.4431 ^{+0.0037} _{-0.0036}	0.0222 ^{+0.0018} _{-0.0018}	3.42 ^{+0.28} _{-0.18}	11.8 ^{+1.9} _{-4.4}	87.6 ^{+8.8} _{-4.1}	0.51 ^{+0.34} _{-0.35}
148340346			10.53	2.73	5441 ± 122	ERG	2.4233 ^{+0.00075} _{-0.00061}	2204.2 ^{+0.0067} _{-0.0101}	0.0195 ^{+0.0025} _{-0.0015}	5.82 ^{+0.57} _{-0.45}	4.03 ^{+0.57} _{-1.1}	83.3 ^{+4.8} _{-6.9}	0.48 ^{+0.31} _{-0.33}

SG: sub-giant sub-population ; ERG: early red giant sub-population

Planet references: TOI-329 b Polanski et al. (2024) ; HD 89345 b Van Eylen et al. (2018) ; TOI-1736 b Akana Murphy et al. (2023)

APPENDIX B: NEWLY DETECTED PLANET CANDIDATE LIGHT CURVES

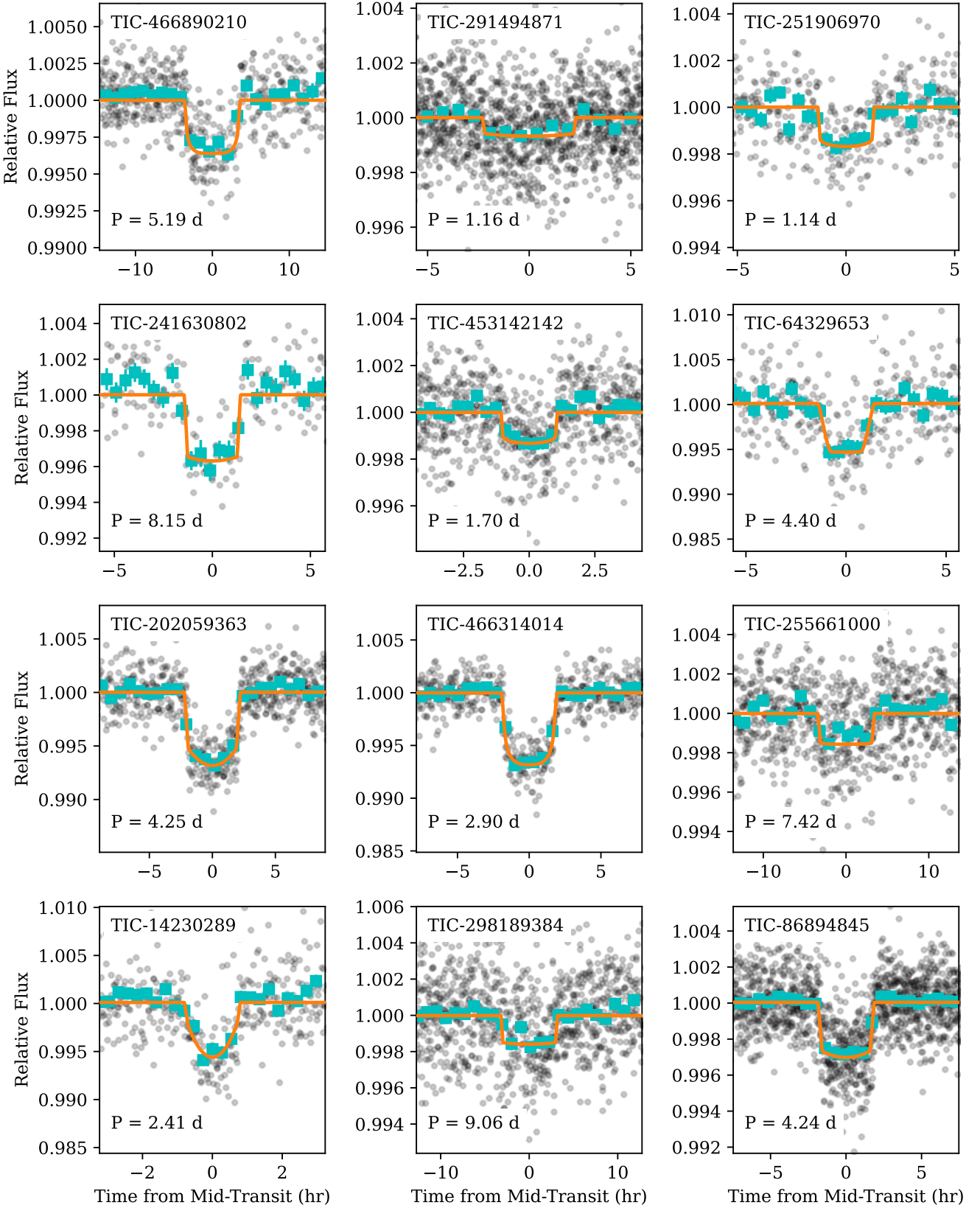


Figure B1. Phase-folded QLP LCs of the new planet candidates we detect in this work. The data is phase-folded using the best fit ephemerides from the transit fitting presented in Section 3.4 and the orange line shows the best fit transit model from the same analysis. The cyan squares show the data binned in phase. The bin width is determined for each object such that there are 6 binned points per transit duration. The annotations on each axis give the TIC ID of the host star and orbital period of each candidate. Note that we show a zoomed in view around phase 0 for visual clarity of each transit event. The full phase-folded flux data sets extend beyond the edges of each panel.

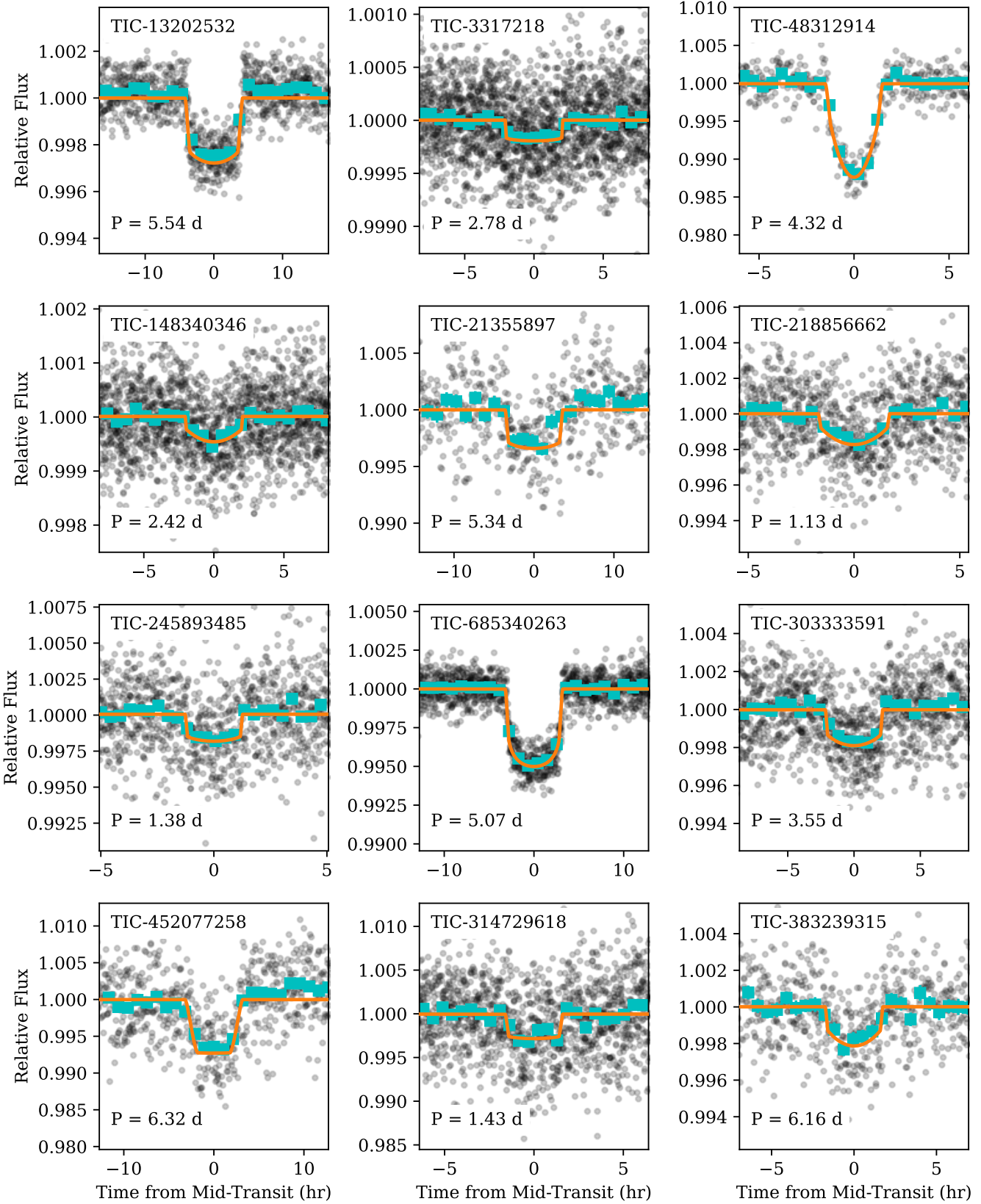


Figure B1. Cont.

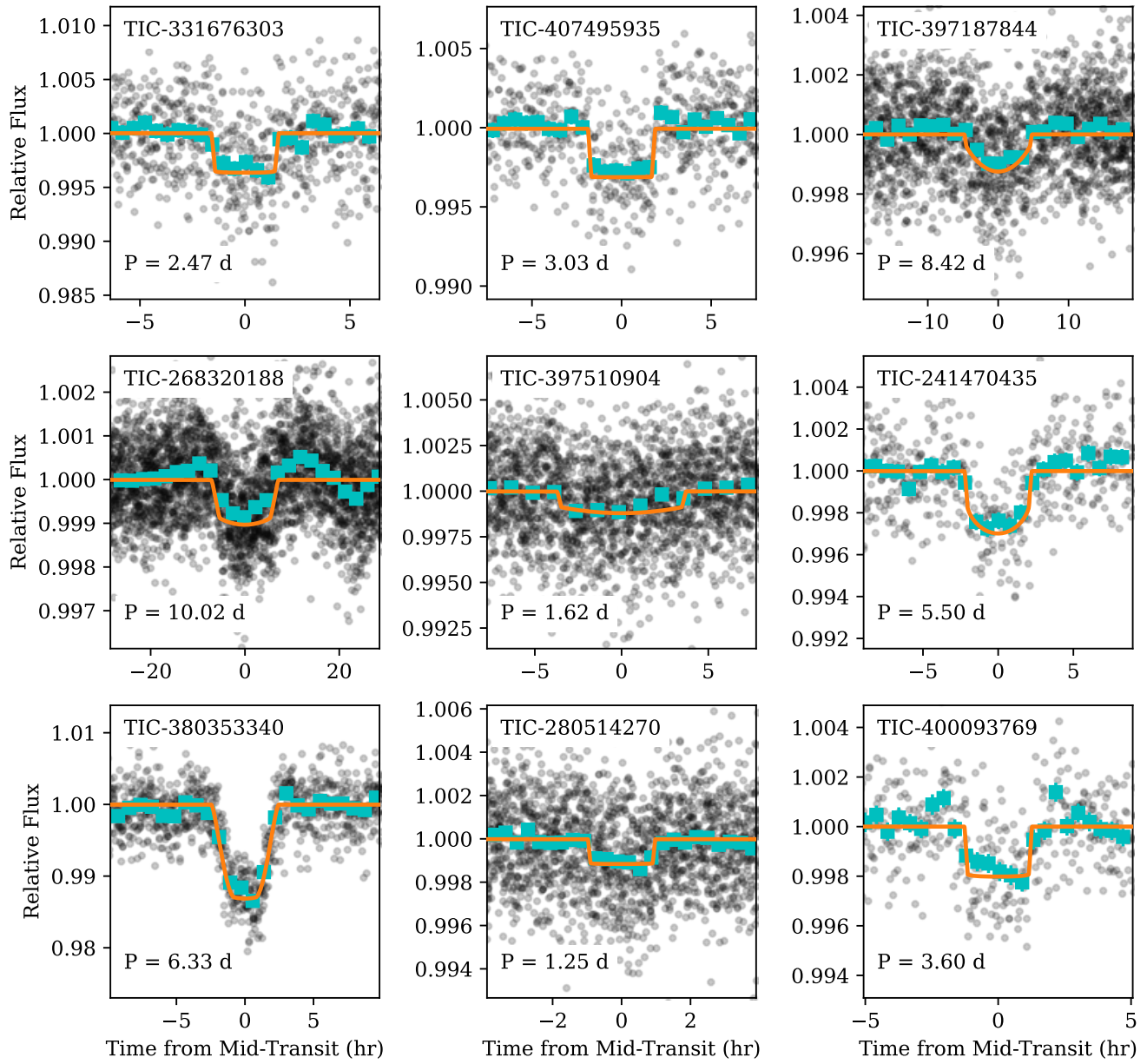


Figure B1. Cont.

This paper has been typeset from a $\text{\TeX}/\text{\LaTeX}$ file prepared by the author.